JOURNAL OF GEOPHYSICAL RESEARCH, VOL. 110, E01003, doi:10.1029/2004JE002327, 2005

A volcanic interpretation of Gusev Crater surface materials from thermophysical, spectral, and morphological evidence

Sara Martínez-Alonso,[1] Bruce M. Jakosky,[1,2] Michael T. Mellon,[1]
and Nathaniel E. Putzig[1,2]

Received 21 July 2004; revised 31 August 2004; accepted 11 November 2004; published 26 January 2005.

[1] Gusev Crater, the Mars Exploration Rover Spirit landing site (160 km diameter; 14.5°S, 184.5°W), has been identified in previous studies as a prime site of geological and exobiological interest on the basis of its potential for having hosted a fluviolacustrine environment; such environment may have been favorable for the development of biological activity. The origin and nature of the materials present at the surface of Gusev Crater are still being debated. In previous studies based on geomorphological and thermophysical data, surface materials in the crater have been interpreted as originating from fluviolacustrine, volcanic, or aeolian processes, or combinations thereof. We present results from the analysis of newly compiled thermophysical (Thermal Emission Spectrometer (TES) and Thermal Emission Imaging System (THEMIS)), spectroscopic (TES), and visible (THEMIS and Mars Observer Camera) data for the Gusev region. These data were analyzed using a new mosaicking technique developed to match the values of contiguous scenes and to produce seamless mosaics apt for geological interpretation. Thermophysical, spectroscopic, and morphological evidence point to the presence of local outcrops of lava flows of basaltic composition, materials consistent with a regolith developed from basaltic materials, fine-grained deposits of basaltic composition strongly modified by wind erosion, and wind deposits. According to these findings, we conclude that most of the materials occupying the present surface of Gusev have characteristics consistent with those of volcanic and aeolian deposits. Fluviolacustrine deposits proposed by other authors may exist under the volcanic materials and may be exposed in impact craters.

Citation: Martínez-Alonso, S., B. M. Jakosky, M. T. Mellon, and N. E. Putzig (2005), A volcanic interpretation of Gusev Crater surface materials from thermophysical, spectral, and morphological evidence, *J. Geophys. Res.*, *110*, E01003, doi:10.1029/2004JE002327.

1. Introduction

[2] On 4 January 2004, the Mars Exploration Rover (MER) Spirit landed successfully in Gusev Crater. This site was selected for one of the two MER landers because of its potential for hosting fluviolacustrine deposits [*Schneeberger*, 1989; *Grin and Cabrol*, 1997; *Cabrol et al.*, 1993, 1998, 2000; *Kuzmin et al.*, 2000]; the origin and nature of the materials present at the surface of Gusev Crater are still being debated.

[3] Gusev is a 160-km crater of Noachian age [*Kuzmin et al.*, 2000] centered at 14.5°S, 184.5°W (Figure 1), with a present average depth of 1.9 km with respect to the surrounding plains and an initial crater depth of 3.1 to 4.6 km as estimated by *Milam et al.* [2003]. Gusev is located within heavily cratered and dissected materials of Noachian and Hesperian age. Large Hesperian channels [*Kuzmin et al.*, 2000], such as Ma'adim Vallis and Durius Vallis, incise this unit. Ma'adim Vallis is the proposed conduit for the water and sediments that putatively filled Gusev, either by active drainage over an extended period of time [*Cabrol et al.*, 1998] or by catastrophic flow [*Irwin et al.*, 2002]. The global dichotomy boundary, located approximately 50 km north of Gusev, separates the southern cratered highlands from the northern lowlands volcanic materials. Hesperian lava flows, heavily dissected by braided channels, and ignimbrites erupted from Apollinaris Patera [*Robinson et al.*, 1993] can be found directly north of Gusev. Volcanosedimentary materials [*Scott and Tanaka*, 1982; *Greeley and Guest*, 1987] of Amazonian age, strongly modified by aeolian erosion, cover the terrains northeast of Gusev. Northwest of Gusev the Apollinaris Patera materials have been affected by sapping due to melting of underground ice or to withdrawal of under-

---

[1] Laboratory for Atmospheric and Space Physics, University of Colorado, Boulder, Colorado, USA.

[2] Also at Department of Geological Sciences, University of Colorado, Boulder, Colorado, USA.

Copyright 2005 by the American Geophysical Union.
0148-0227/05/2004JE002327$09.00

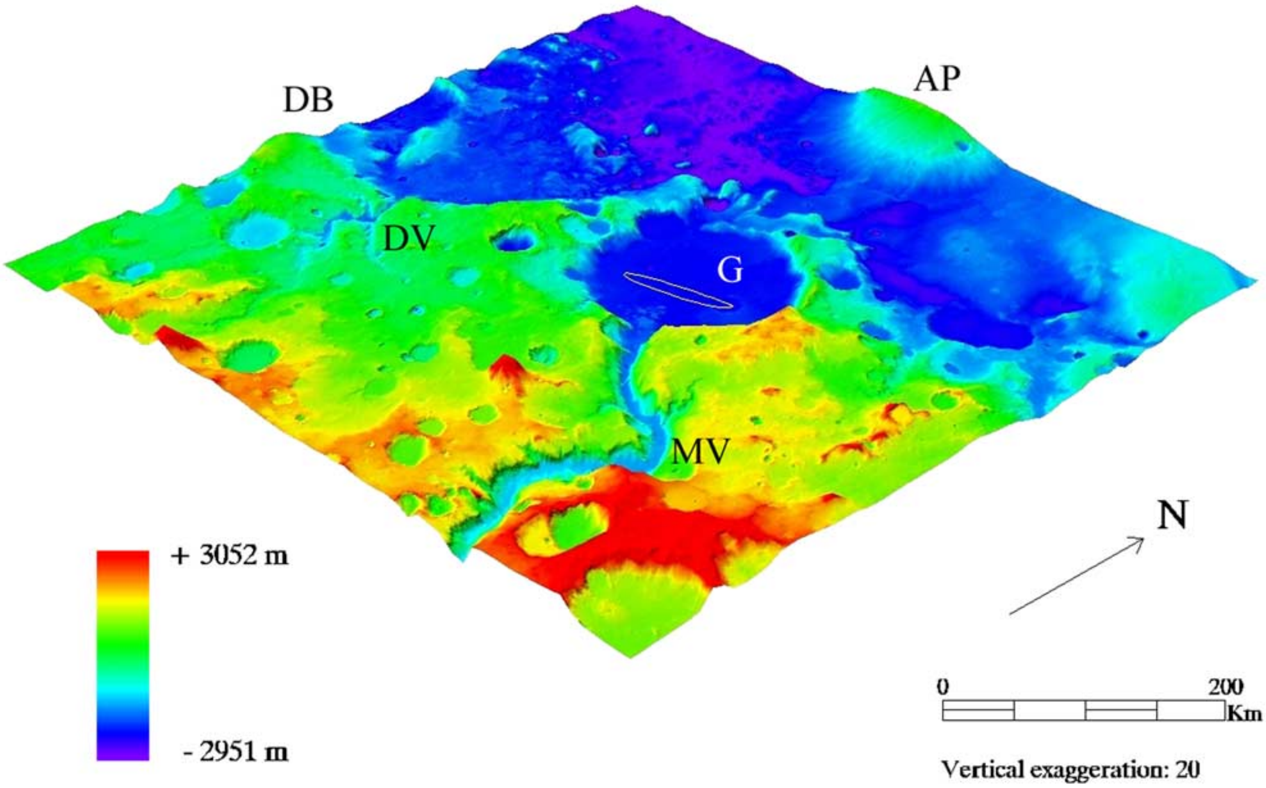

Figure 1. Regional MOLA topography including the study area. DB, dichotomy boundary; AP, Apollinaris Patera; DV, Darius Vallis; MV, Ma'adim Vallis; G, Gusev Crater. The MER-Spirit landing ellipse is shown for reference.

ground magma, both consistent with nearby Apollinaris Patera, producing chaotic/fretted terrains Hesperian and Amazonian in age [*Kuzmin et al.*, 2000].

[4] Previous geomorphologic studies of the Gusev region based on Viking imagery include those of *Scott et al.* [1978], *Schneeberger* [1989], *Grin and Cabrol* [1997], *Cabrol et al.* [1993, 1998, 2000], and *Kuzmin et al.* [2000]. The thermophysical properties of this area, as derived from Mars Global Surveyor Thermal Emission Spectrometer (MGS-TES) [*Christensen et al.*, 1992] bolometric data following the method described by *Mellon et al.* [2000], were studied previously by *Jakosky and Mellon* [2001], although very restricted spatial coverage limited the results obtained in that study. *Milam et al.* [2003] carried out a detailed study of the Gusev Crater basin, based on morphologic analysis of visible and infrared imagery from the Mars Odyssey Thermal Emission Imaging System (THEMIS) [*Christensen et al.*, 2003] and the MGS-Mars Observer Camera (MOC) [*Malin et al.*, 1992], topographic data from the MGS-Mars Observer Laser Altimeter (MOLA) [*Zuber et al.*, 1992], and thermophysical data. In their study, *Milam et al.* [2003] identified thermophysical units in Gusev Crater based on the qualitative comparison of TES albedo and THEMIS nighttime and daytime brightness temperatures; TES-derived thermal inertia published by *Jakosky and Mellon* [2001] was also included in their analysis. P.R. Christensen et al. (Mars Exploration Rover candidate landing sites as viewed by THEMIS, submitted to *Icarus*, 2004, hereinafter reffered to as Christensen et al., submitted manuscript, 2004) reviewed the morphological and thermal properties of the Gusev landing site through the analysis of THEMIS visible imagery and THEMIS-derived daytime and nighttime temperature data. A subsequent analysis of the thermophysical properties of surface materials in the Gusev region (from 10°S, 190°W, to 20°S, 180°W), based on newly compiled data including TES albedo and thermal inertia mosaics, as well as THEMIS radiance, brightness temperature, and thermal inertia mosaics, is included in the work of B. M. Jakosky et al. (Thermophysical properties of the MER and Beagle II landing sites on Mars, submitted to *Journal of Geophysical Research*, 2004, hereinafter referred to as Jakosky et al., submitted manuscript, 2004).

[5] The nature and origin of the materials covering Gusev Crater is still controversial. *Scott et al.* [1978] hypothesized that Gusev is covered by an "eolian deposit, moderately thick cover over lava flows." Following studies by *Schneeberger* [1989], *Grin and Cabrol* [1997], *Cabrol et al.* [1993, 1998, 2000], and *Kuzmin et al.* [2000] favored a fluviolacustrine origin for these deposits. *Rice and Christensen* [2003] proposed a mixture of debris flow activity and volcanic ash deposition. *Milam et al.* [2003] and Christensen et al. (submitted manuscript, 2004) stated that aqueous, aeolian, volcanoclastic processes, or a mixture of all the above, could explain the surface materials in this region.

[6] Here we analyze the thermophysical, spectroscopic, and geomorphologic properties of the surface deposits of Gusev Crater utilizing TES, THEMIS, MOC, and MOLA

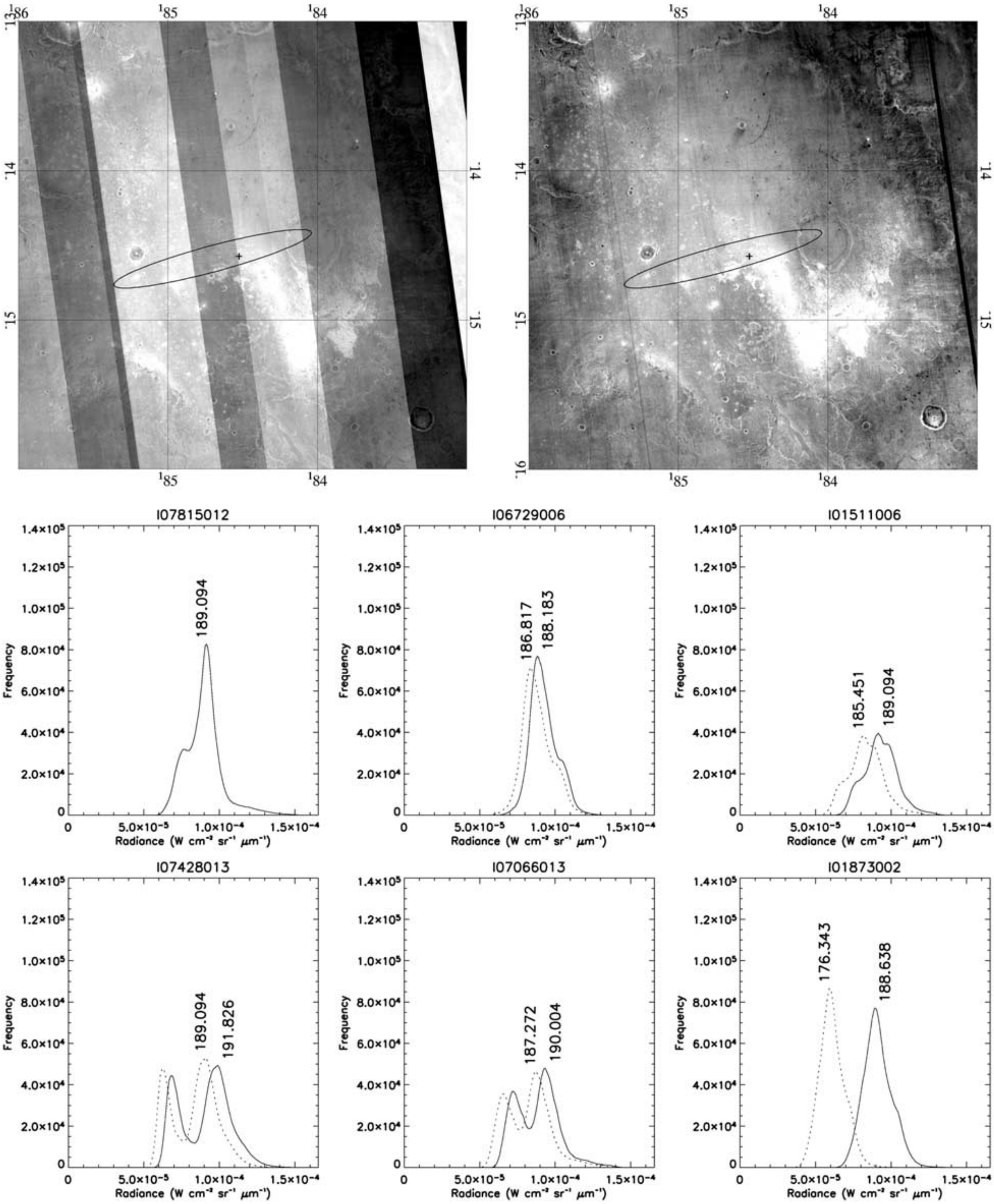

Figure 2. The top panels show THEMIS night radiance mosaics of the study (left) before and (right) after applying the mosaicking procedure described in the text; landing ellipse and landing site are shown for reference. The bottom panels show the mosaicking processing effect on the radiance distribution of the six THEMIS scenes that cover the landing ellipse (scene identifier shown on top of each panel). Scene I07815012 was the "control" for this block of scenes and therefore remained unchanged. Radiance histograms for each scene are shown with dotted lines (original) and solid lines (processed). Labels on histogram peaks correspond to their brightness temperature in Kelvin.

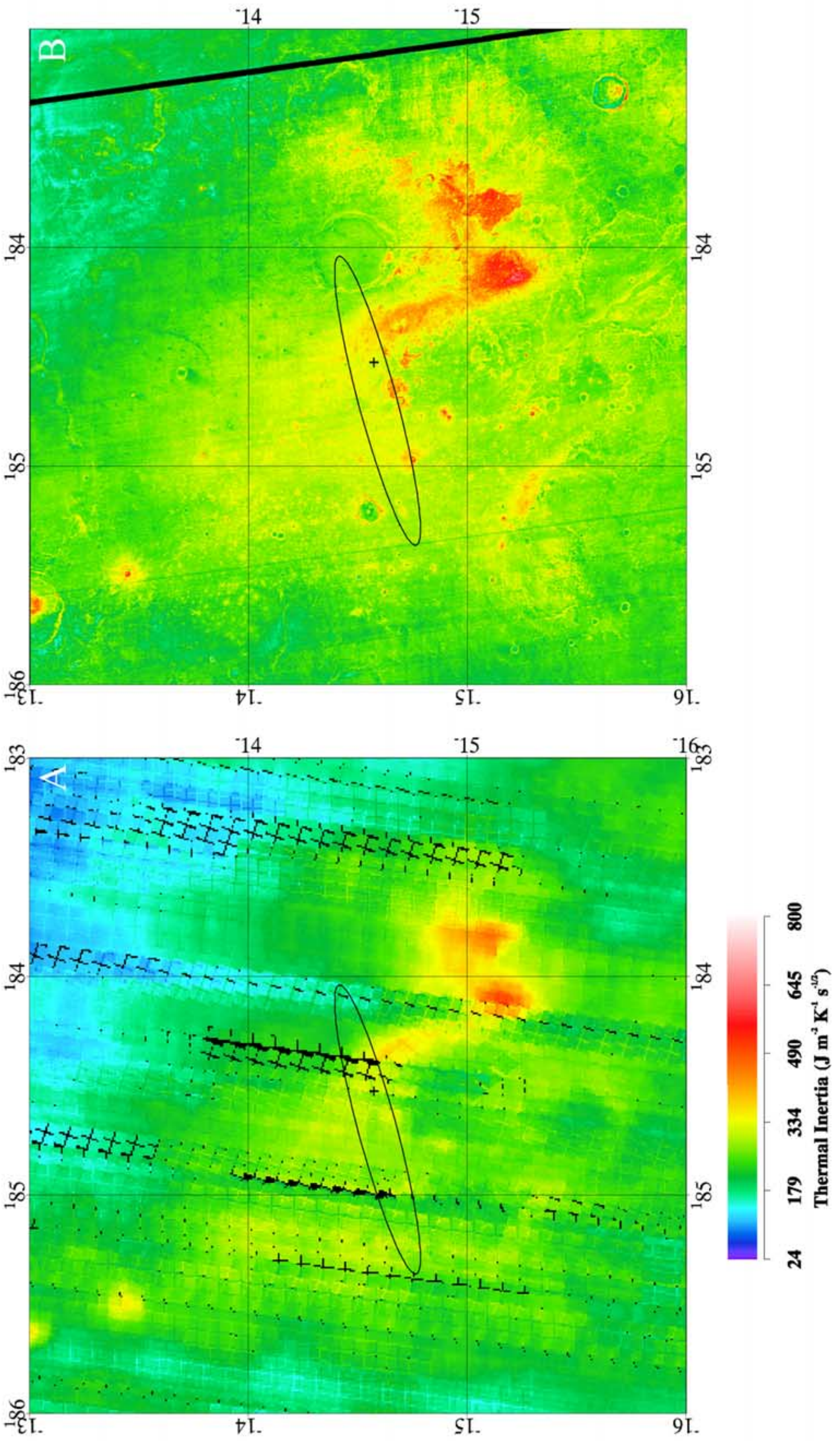

Figure 3. (a) TES-derived thermal inertia map of the study area. (b) THEMIS-derived thermal inertia map of the same area. While Figure 3b shows higher spatial resolution, the uncertainty of the inertia values calculated is also higher (see text for explanation).

data. From this analysis we derive an alternative interpretation of the geological processes that produced these deposits.

2. Methodology

[7] We present results from the analysis of newly compiled data for Gusev Crater. These data include TES-derived albedo, thermal inertia, and emissivity mosaics, as well as THEMIS radiance, brightness temperature, and thermal inertia mosaics. MOLA topographic data, and visible THEMIS and MOC imagery have been also utilized in this study. To facilitate their synergic analysis, all these data sets have been rectified to fit the simple cylindrical projection and areocentric coordinate system as defined in the IAU2000 report [*Seidelmann et al.*, 2002]. Longitudes are given in degrees west of the prime meridian and all figures are oriented with north up, unless noted otherwise. In this section we present the mosaicking procedure applied to the THEMIS data, as well as the data sets employed and the methodologies followed in our thermophysical and spectroscopic analyses.

2.1. Mosaicking Procedure

[8] Radiance data measured over adjacent regions, or over a single region at different times, have different values due to changing atmospheric conditions, differences in illumination, and instrument performance, among other factors. Derivation of thermal inertia should correct all of these issues and produce seamless mosaics without further adjustment between scenes; the fact that it does not may be indicative of unresolved issues in the thermal inertia derivation scheme (Jakosky et al., submitted manuscript, 2004). In order to match THEMIS radiance, brightness temperature, and thermal inertia images of adjacent regions and produce seamless mosaics suitable for geological interpretation, we have developed the methodology described here. This technique is not intended to produce accurate absolute values but reasonable relative values appropriate for geologic analysis.

[9] First, THEMIS band-9 (12.6 μm) infrared scenes of the study area were selected according to their quality (i.e., no missing lines, no obvious artifacts) and low TES-derived atmospheric dust and water-ice opacities [*Smith et al.*, 2001] (opacities cannot be derived from THEMIS data; however, TES data show that dust and ice opacities follow clear trends along time, allowing for the reliable interpolation of opacities in between TES observations). Daytime images were selected also according to season to avoid large illumination differences. Next, the individual THEMIS calibrated radiance scenes were map-projected with Integrated Software for Imagers and Spectrometers (ISIS; *Eliason* [1997], *Gaddis et al.* [1997], *Torson and Becker* [1997]) and filtered to correct calibration artifacts (J. Bandfield, personal communication, 2003). We then processed blocks of contiguous, overlapping, map-projected THEMIS calibrated radiance scenes by identifying the spatial overlap between pairs of scenes, calculating a linear regression between the overlapping regions, and applying that regression to force the radiance of one scene to match that of the other (the "control" scene). Linear regression was found to be an adequate approximation to account for major radiance differences between multitemporal scenes covering the same area. The control scene was selected on a case-by-case basis, in most cases choosing that scene with the highest radiance values (and therefore with the highest brightness temperature), which should have the highest signal-to-noise ratio. The original radiance values of the control scene remained unchanged. Once a linear transformation was applied to a scene, that scene was not processed further. The average radiance of processed blocks of THEMIS scenes and/or single THEMIS scenes that did not overlap spatially were adjusted to that of a specific block or scene, or to a user-specified radiance value. Finally, the scenes resulting from this processing were assembled into the mosaic image.

[10] This method preserves the radiance frequency distribution of the images processed, and produces acceptable net changes in radiance. In the example shown in Figure 2, the difference in temperature between original and radiance-adjusted scenes ranges between 1.37 and 12.30 K, with an average of 4.55 K. Radiance values in the study area were adjusted to match best those at the center of the landing ellipse in THEMIS scenes considered representative and chosen as the control ones, therefore remaining unchanged. By applying this method, we are effectively normalizing the individual scenes to a common set of local times (diurnal effects) and atmospheric conditions (seasonal effects), although trading some absolute accuracy for mosaic coherence, since diurnal and seasonal temperature cycles are nonlinear in time. However, nonlinear effects are minimal because (1) the relationship between radiance and brightness temperature is quasi-linear for the range of radiance values in the data analyzed ($0.87 \cdot 10^{-4}$ to $1.59 \cdot 10^{-4}$ W cm^{-2} sr^{-1} μm^{-1}) and thus the maximum errors in temperature introduced by using a linear approximation are below 1 K; and (2) the relationship between thermal inertia and surface temperature is quasi-linear for the acquisition times of the data utilized (between Mars hours 3.2 and 5.4).

2.2. Thermophysical Properties Analysis

[11] A thermal inertia map derived from nighttime bolometric brightness temperatures was obtained from TES data (Figure 3a) utilizing the model described by *Mellon et al.* [2000]; a higher spatial resolution map of THEMIS thermal inertia (Figure 3b) was derived utilizing the same model, modified as described by Jakosky et al. (submitted manuscript, 2004). In order to produce a seamless THEMIS thermal inertia map, the model was applied to a band-9 THEMIS calibrated radiance mosaic produced as described in the previous section, converted to nighttime brightness temperatures following a lookup table–based procedure [*Christensen et al.*, 2003, 2004]. This approach was found to produce results analogous to those obtained by mosaicking the individual thermal inertia images.

[12] The total uncertainties for thermal inertia derived from applying the nighttime bolometric temperatures model to TES data were estimated previously to be 6% [*Mellon et al.*, 2000]. For THEMIS-derived thermal inertia, the estimated uncertainties are in the 25% range (Jakosky et al., submitted manuscript, 2004). Consequently, in this analysis, only TES-derived thermal inertia values were utilized quantitatively; THEMIS-derived thermal inertia values were utilized for detailed qualitative spatial analysis, because of

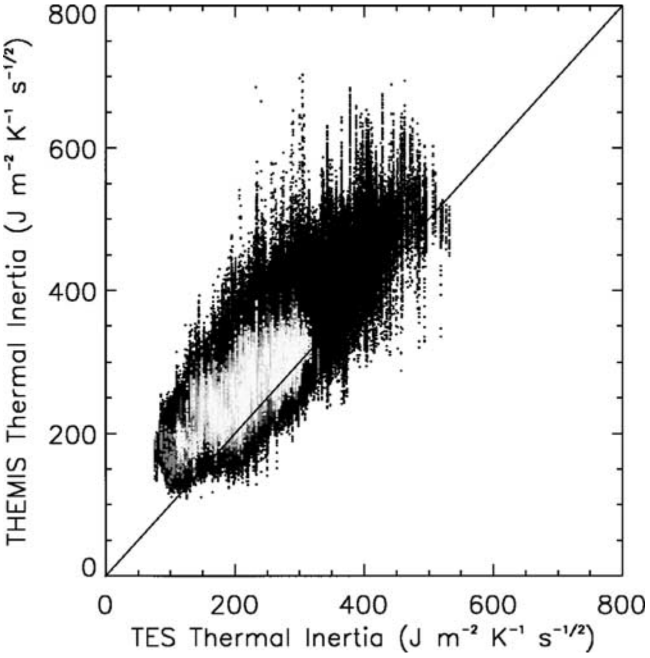

Figure 4. Two-dimensional histogram comparing TES- and THEMIS-derived thermal inertia values for the study area. Lighter gray levels in the data cloud indicate higher frequencies. The data distribution follows a linear trend parallel to the 1:1 line. THEMIS thermal inertia values are higher than the TES-derived by approximately 50 J m^{-2} K^{-1} $s^{-1/2}$. The vertical scatter in the plot may be explained by superior THEMIS spatial resolution, emissivity effects on the THEMIS spectra-derived temperatures, differences in spatial resolution between the THEMIS data and ancillary data used to calculate thermal inertia, and instrument uncertainties.

their superior spatial resolution. Thermal inertia values derived from both data sets for the Gusev study area present a good linear correlation, as shown in Figure 4. The two-dimensional histogram distribution follows a linear trend, parallel to the 1:1 line. In this example THEMIS thermal inertia values are higher than those derived from TES data by approximately 50 J m^{-2} K^{-1} $s^{-1/2}$ (hereafter, thermal inertia units of J m^{-2} K^{-1} $s^{-1/2}$ will be assumed). This observation is consistent with similar results obtained previously (Jakosky et al., submitted manuscript, 2004).

[13] Thermal inertia and albedo values were utilized to determine physical properties of surface materials such as particle size, rock/bedrock exposure, and degree of induration; these properties constrain the physical character of the surface and the geological context of the materials identified from the analysis of the spectral data. The physical properties of Gusev's surface materials were determined in comparison to the global thermophysical units defined by *Mellon et al.* [2000] and *Putzig et al.* [2004]. *Mellon et al.* [2000] observed the presence of three modes of frequent correlation, the first two of which had been previously observed in Viking data by *Palluconi and Kieffer* [1981]: unit A, of low thermal inertia and high albedo, interpreted as dominated by bright, unconsolidated materials; unit B, with high thermal inertia and low albedo, interpreted as dominated by coarse materials (sand, rocks, bedrock) and some duricrust; and unit C, of moderate-to-high thermal inertia and intermediate albedo, interpreted as an indurated material with some sand, rocks, and bedrock. *Putzig et al.* [2004] incorporated additional TES data and refined this classification by adding 4 new units (D-G). Figure 5 represents the distribution of global albedo and thermal inertia (frequency of occurrence shown with contour lines) and those corresponding to the Gusev study area (frequency of occurrence in shades of gray). A large proportion of the surface of Gusev coincides with unit C of *Mellon et al.* [2000]; units A and B are also present in the study area.

[14] In order to depict subtle differences in surface materials due to diurnal temperature variations and surface albedo, allow for the recognition of surface morphologies associated with such materials, and provide a global and spatially continuous view of the study area, a false-color image was produced combining the THEMIS-derived nighttime and daytime brightness temperature mosaics produced in this study and a subset of the MOC red band wide-angle mosaic produced by M. C. Malin et al. (available at http://www.msss.com/mgcwg/mgm). The three images were coregistered to account for minor misalignments among them, and the MOC mosaic was resampled to match the higher spatial resolution of the THEMIS data (100 m/pixel). The resulting false-color image (Figure 6), which provides close-to-full coverage of the study area, was analyzed in conjunction with the TES- and THEMIS-derived thermal inertia mosaics, as well as with a TES-derived calibrated albedo map to determine the thermophysical properties of the surface materials at Gusev. Thermophysical units were defined in the TES thermal inertia versus TES albedo two-

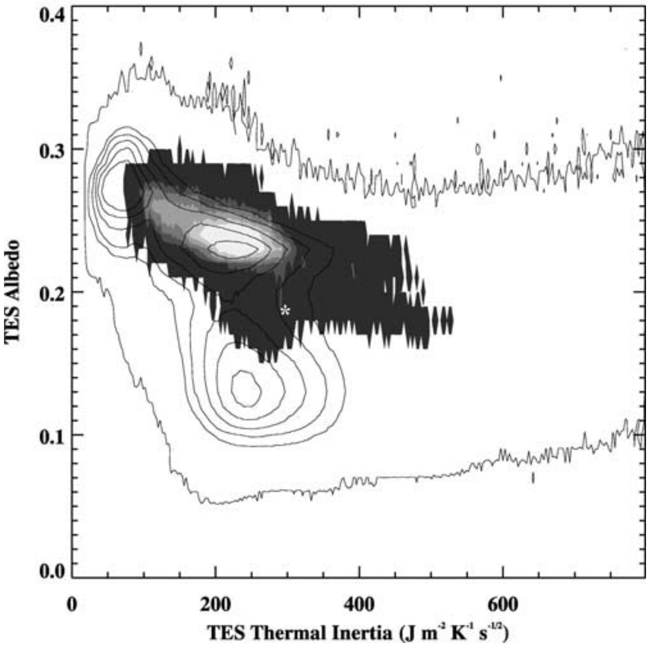

Figure 5. TES albedo and TES-derived thermal inertia values for Gusev Crater (frequency of occurrence in shades of gray; lighter gray levels indicate higher frequencies) versus Mars global values (black contour lines). The asterisk denotes the values calculated for the MER-Spirit landing site (TES albedo, 0.187; TES thermal inertia, 300).

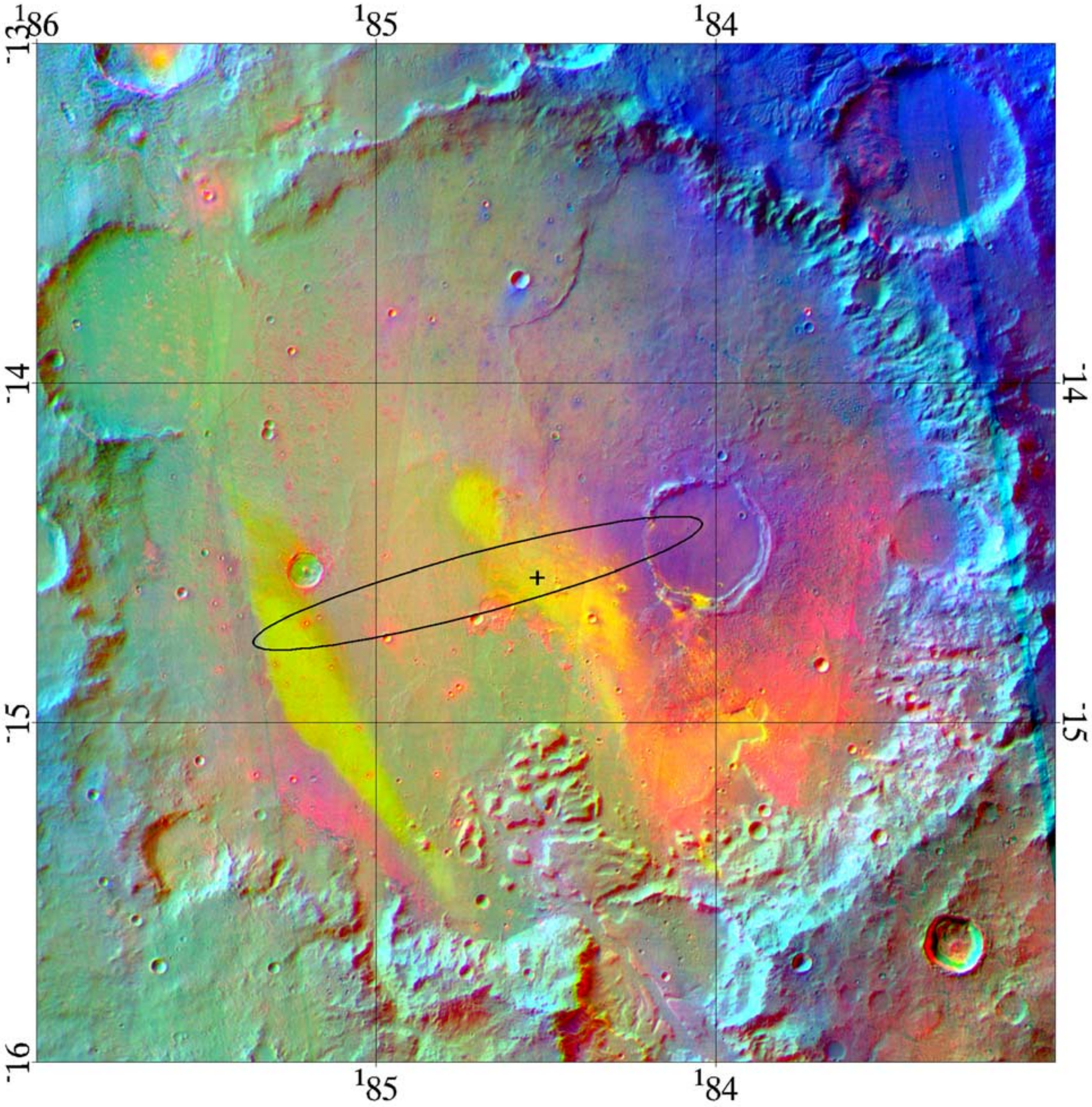

Figure 6. False color image showing the main thermophysical units at Gusev Crater. Red band: THEMIS night temperature mosaic. Green band: THEMIS day temperature mosaic. Blue band: MOC red wide-angle mosaic.

dimensional histogram (Figure 7a) and subsequently mapped back into the spatial domain (Figure 7b) to analyze their areal distribution and morphological characteristics. TES- and THEMIS-derived thermal inertia values show the same thermophysical units; THEMIS allows for better spatial delineation of these units and detection of smaller occurrences.

2.3. Spectral Properties Analysis

[15] TES measures spectral radiance in 143 (single-scan mode) or 286 (double-scan mode) spectral bands spanning the 148 to 1715 cm^{-1} range (5.8 to 67.6 μm). The spatial resolution of each single-scan spectrum is approximately 3 by 6 km. Spectral emissivity is computed by dividing calibrated radiance by the Planck curve of a blackbody at the maximum brightness temperature (within the 300 to 1350 cm^{-1} range) derived for each spectrum [*Christensen et al.*, 2001]. We present results derived from the analysis of TES single-scan emissivity data available for this region to date (orbits 1583 to 21003). TES double-scan emissivity data corresponding to the same orbit range of lower spatial resolution were also utilized to corroborate results obtained in the analysis of the single-scan data.

[16] Daytime TES spectral data available for the study area were filtered according to several quality criteria: no

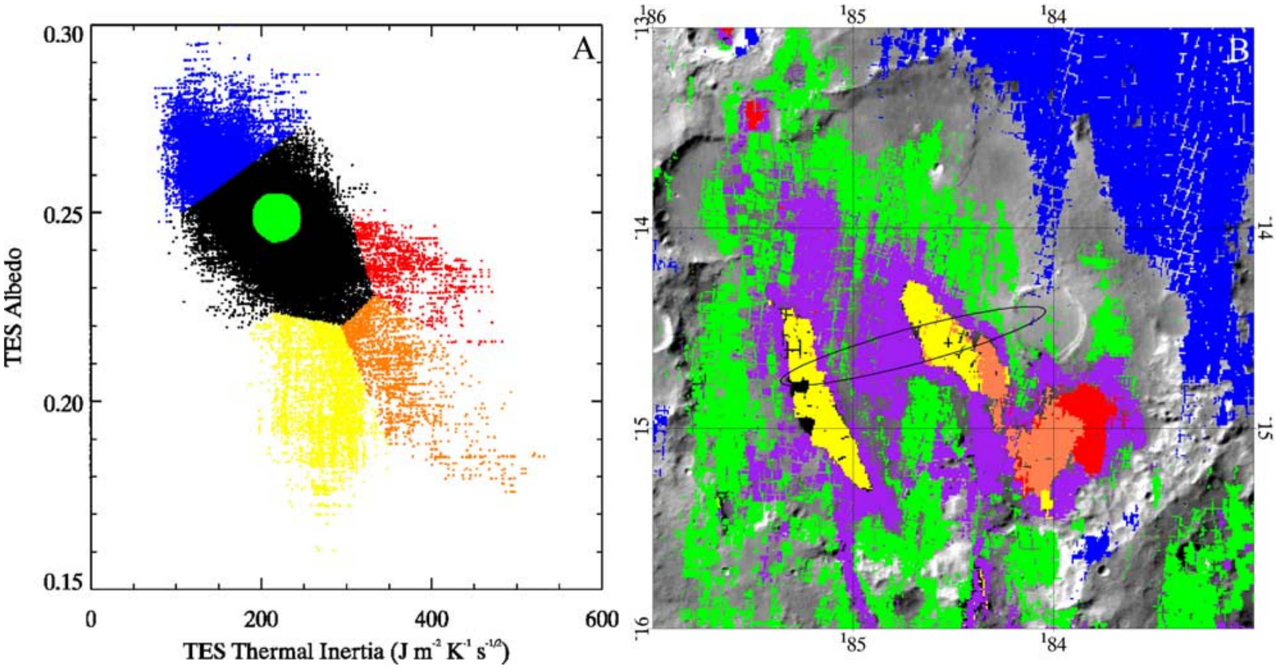

Figure 7. (a) Thermophysical units derived according to TES albedo and TES thermal inertia values. Blue (LTI), low thermal inertia; yellow (LA), low albedo; red (HTIR), high thermal inertia rough; orange (HTIS), high thermal inertia smooth; green (PM), plains materials. Black areas in the two-dimensional histogram were not mapped. (b) Spatial distribution of the TES-derived thermophysical units superimposed to MOC visible data. Same color scheme as in Figure 7a: purple indicates transitional materials with properties intermediate between these of the plains materials unit and the high thermal inertia units.

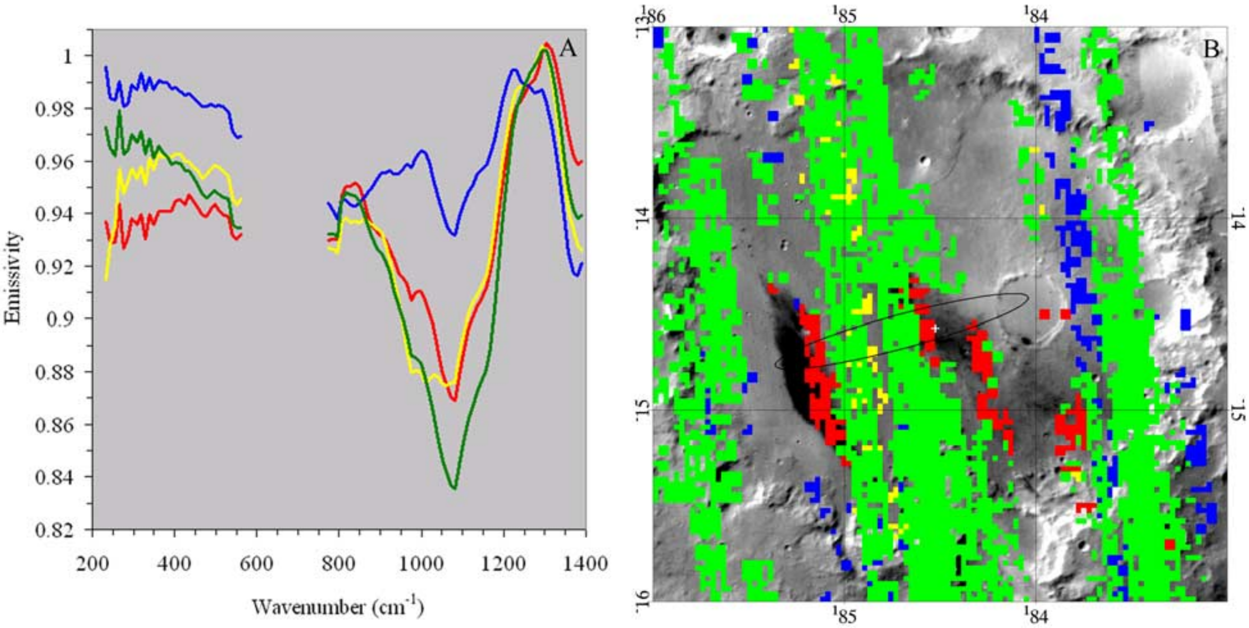

Figure 8. (a) TES-derived spectral endmembers utilized as reference spectra in the classification of the emissivity data. Red, surface type 1 (materials of basaltic composition); green, dust; blue, atmospheric water ice; yellow, instrument noise. (b) Result of the classification: spatial distribution of the closest matches to the TES-derived spectral endmembers superimposed to MOC visible data. Same color scheme as in Figure 8a. The water-ice unit is located within a few single TES orbital groundtracks, indicating the atmospheric character of this class. The noise endmember is restricted to a few groundtracks subsequent to TES orbit 7000.

Table 1. TES Thermal Inertia, Albedo, and Dominating Spectral Characteristics of the Thermophysical Units Defined in This Study

Thermophysical Unit	TES Albedo[a]	TES Thermal Inertia,[a] J m^{-2} K^{-1} $s^{-1/2}$	TES Spectral Characteristics
Low thermal inertia (LTI)	0.25–0.30 (0.27 ± 0.007)	76–266 (141 ± 28)	dust
Low albedo (LA)	0.16–0.22 (0.20 ± 0.012)	186–347 (275 ± 28)	surface type 1 (basaltic composition)
High thermal inertia rough (HTIR)	0.21–0.25 (0.24 ± 0.007)	308–483 (366 ± 38)	surface type 1 (basaltic composition)
High thermal inertia smooth (HTIS)	0.17–0.23 (0.21 ± 0.011)	295–532 (356 ± 41)	surface type 1 (basaltic composition)
Plains materials (PM)	0.24–0.25 (0.25 ± 0.003)	192–245 (218 ± 13)	dust

[a] Albedo and thermal inertia given as follows: minimum-maximum (average ± standard deviation).

spatial or spectral averaging, close-to-nadir acquisition geometry, low atmospheric dust and ice opacities, brightness temperatures equal to or greater than 250 K for maximum signal to noise, and instrument performance. The spectra acquired by each of the 6 TES detectors were resampled to a common set of wave numbers and full width at half maximum. Noisy spectra dominated by saw- and sine-like artifacts were identified and discarded [*Martínez-Alonso et al.*, 2003a]. When more than one TES observation that met our quality criteria existed for a single field-of-view, the first observation was utilized to avoid instrument noise that has increased with time. The resulting TES emissivity data set covered close to 60% of the study area.

[17] The single- and double-scan TES data were examined using constrained linear mixing models; the spectral endmembers necessary to explain the spectral variability present in the data were extracted from the data themselves. To determine the spectral dimensionality of the TES data, segregate noise, and reduce the computational requirements for subsequent processing, the Minimum Noise Fraction (MNF) transformation [*Green et al.*, 1988; *Boardman and Kruse*, 1994] was applied to the data. Noise statistics were obtained from TES internal black body measurements following the technique described by *Martínez-Alonso et al.* [2003a]. The purest spectra or endmembers in the scene (these that cannot be explained by linear combinations of other spectra in the data set) were extracted utilizing the Pixel Purity Index technique [*Boardman et al.*, 1995] (Figure 8a). In order to accept that an endmember had spectral significance, repeated observations (performed at different times in the same location or in adjacent locations) were always required. Once the spectral endmembers were extracted, they were identified by comparison to public spectral libraries (ASTER Spectral Library, Jet Propulsion Laboratory, California Institute of Technology; *Christensen et al.* [2000]) and results from previous studies [*Bandfield et al.*, 2000; *Smith et al.*, 2000]. The spatial distribution of the closest matches to these spectral endmembers was established applying the Spectral Angle Mapper algorithm [*Kruse et al.*, 1993] (Figure 8b). This technique determines the spectral similarity between two spectra (unknown and reference) by calculating the angle between them, treating them as vectors in an *n*-dimensional space (n being the number of spectral bands); smaller angles represent closer matches to the reference spectra (the TES-derived endmembers).

3. Results

[18] From detailed combined analysis of their albedo and thermal inertia properties, the following thermophysical units were identified (Figure 7; their thermal inertia, albedo, and dominating spectral characteristics are summarized in Table 1):

[19] 1. Low thermal inertia unit (LTI), located in the northeastern corner of Gusev and adjacent area outside the crater. This unit presents high albedo (0.25 to 0.30) and the lowest thermal inertia values in the crater (76 to 266).

[20] 2. Low albedo (LA) unit presents the lowest albedo values in the region (0.16 to 0.22) and intermediate thermal inertia (186 to 347). This unit appears along two large, subparallel NW-SE dark stripes, in smaller outcrops in the southern side of the Thira crater rim (centered near 14.5°S, 184.1°W), and locally on the units to the south of Thira.

[21] 3. High thermal inertia, morphologically rough unit (HTIR), comprises a large, continuous region southeast of Thira crater. This unit has low-to-intermediate albedo (0.21 to 0.25), and high thermal inertia (308 to 483); it presents very distinct rough, etched, surface morphology.

[22] 4. High thermal inertia, morphologically smooth unit (HTIS), present south and west of Thira. This unit has low-to-intermediate albedo (0.17 to 0.23), and the highest thermal inertia in the study area (295 to 532); its smooth surface morphology contrasts strongly with that of the previous unit.

[23] 5. Plains materials unit (PM). Localized in the periphery of Gusev, and in the northern, western, and northeastern portions of the crater. It presents intermediate thermal inertia (192 to 245) and albedo (0.24 to 0.25).

[24] The spatial boundaries between certain units (e.g., between the HTIR and HTIS units) are sharp. In other cases, there is a continuum of materials with thermophysical properties intermediate between units (e.g., transitional materials between the PM unit and the two high thermal inertia units occupy the central part of Gusev's floor; there is also a continuum between the LTI and PM units).

[25] The four spectral endmembers detected in the TES data (Figure 8a) are consistent with surface type 1

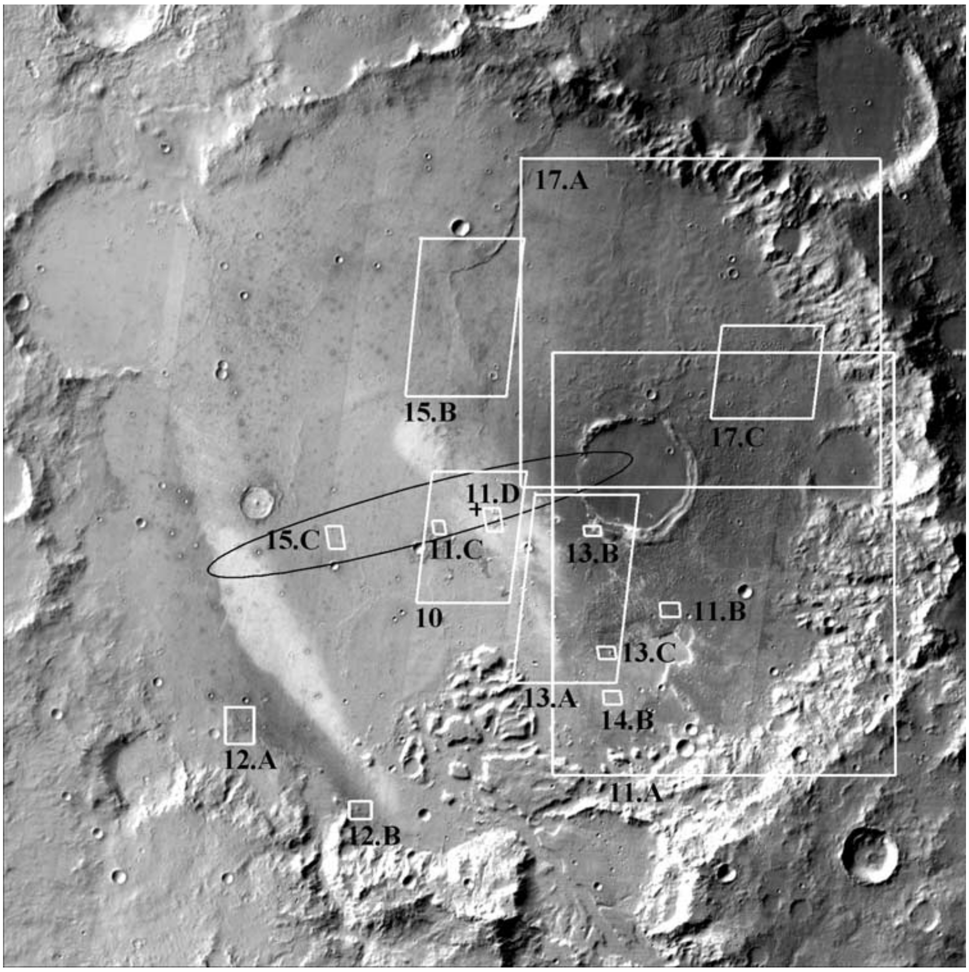

Figure 9. Mosaic of THEMIS daytime brightness temperature images showing the locations of detailed visible MOC and THEMIS scenes discussed later.

[*Bandfield et al.*, 2000] interpreted as a unit of basaltic composition, surface dust, airborne water ice aerosols, and instrument noise (Figure 8). Surface type 1 coincides with the low-albedo and high thermal inertia thermophysical units; it presents locally the highest thermal inertia in the region. The dust unit is widely present in Gusev, coinciding spatially with the PM and LTI thermophysical units. These two thermophysical units represent the highest albedo values and the lowest thermal inertia values in the region; intermediate thermal inertia values present locally could indicate a certain degree of induration. The water-ice unit is located mostly within a few single TES orbital groundtracks, indicating the atmospheric character of this class. The noise endmember occurs along a few orbits subsequent to TES orbit 7000. Repeated observations (from both single- and double-scan data) over the same field of view fail to show the spectral characteristics of this endmember. The noise endmember is consistent with an instrument anomaly of unclear origin, which grew progressively worse after orbit 7000 [*Bandfield*, 2002].

[26] The nature of each of the thermophysical units identified is next fully described by integrating thermophysical and spectroscopic evidence with geomorphological evidence provided by THEMIS and MOC visible imagery (whose locations are shown in Figure 9 for context) and the MOLA elevation model.

3.1. Low Thermal Inertia Unit

[27] The high albedo and low thermal inertia of this unit are consistent with the properties of an unconsolidated dust deposit (unit A of *Mellon et al.* [2000]), locally thermally thin at higher inertia (unit G of *Putzig et al.* [2004]). Its thermal inertia values correspond to grain sizes between 3 and 500 μm (mean near 35 μm) [*Kieffer et al.*, 1973; *Jakosky*, 1986; *Presley and Christensen*, 1997], that is, to unconsolidated silt to medium sand materials, movable by wind. The TES emissivity data corresponding to this unit are consistent with the spectral signature of dust. The surface morphology of this unit is smooth at THEMIS visible scale, disturbed by small craters and subtle sinuous ridges.

[28] There is a smooth transition between the thermophysical properties of the LTI unit and those of the PM unit present in the northeastern quadrant of Gusev (Figures 5, 6, and 7a), as well as morphological continuity at THEMIS infrared scale. One differentiating factor between these two units is the thermophysical signature of small craters (2.5 km in diameter or less) (Figure 6). Unlike in the PM

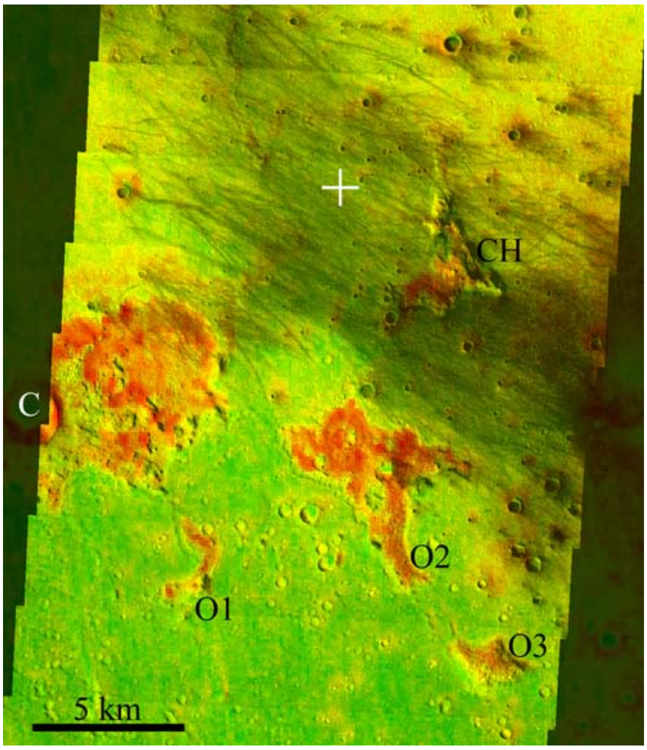

Figure 10. THEMIS visible image V07909002 superimposed on THEMIS-derived thermal inertia map. MER-Spirit landing site shown with a white cross. Red indicates high thermal inertia, yellow and green indicate progressively lower thermal inertia values. Three of the proposed thermophysical units are present in this region: LA unit, characterized by dust-devil tracks; PM unit, of intermediate thermal inertia, with local high values corresponding to small crater ejecta; and HTIR unit, outcropping in the Columbia Hills (CH), around Castril Crater (C) (name provisionally approved by the WGPSN), and in other three discrete outcrops (O1, O2, O3).

unit, in the LTI unit all craters visible in the study area at THEMIS infrared scale (except for one, centered at 13.79°S, 183.73°W) have thermal inertia and albedo similar to these of their surroundings. *Milam et al.* [2003] recognized that, unlike in other parts of Gusev, small craters in this region present floors that appear cold in nighttime thermal infrared data. We interpret the indistinct signature of small craters in the LTI unit as evidence of the late deposition of this unit, as shown by the fact that it has blanketed all but one of the small craters in the region (probably the youngest of its size; this crater appears in Viking scene 088A70, acquired in 09/1976).

3.2. Low Albedo Unit

[29] The LA unit is analogous both in spatial location, albedo, and thermal inertia values to unit LA_t of *Milam et al.* [2003], who interpreted it as consistent with a surface of medium-grained sand.

[30] In this analysis we find that according to its albedo and thermal inertia properties, the LA unit lies between units B and C of *Mellon et al.* [2000]. Therefore it is consistent with a surface dominated by a mixture of indurated material, coarse particles, exposed rocks, or bedrock, and devoid of unconsolidated, high albedo fine materials. The TES emissivity data available for this unit is consistent with type 1 materials, of basaltic composition. Visible imagery illustrates the spatial coincidence between the LA unit and numerous dust devil tracks roughly oriented NW-SE (Figure 10); this unit is very dynamic through time, as shown by multitemporal MOC and THEMIS data as well as by older Viking data [*Milam et al.*, 2003]. Dust devils locally remove fine, bright materials from the surface, unveiling underlying materials of lower albedo but similar thermal inertia. This is in agreement with the observation that the thermal inertia of the LA unit and that of the surrounding PM unit are similar: thermal inertia senses the properties of the top few centimeters and will therefore be little affected by a very thin veneer of dust.

[31] The MER-Spirit landed in the LA unit (landing site coordinates: 14.57°S, 184.53°W; TES thermal inertia: 300; TES albedo: 0.187) and traversed it in its way toward the Columbia Hills (Figure 10). Spirit's observations indicate that this is a regolith characterized by mixtures of rock fragments and fine-grained particles. The rock fragments (that are angular, sometimes faceted, present pits and vugs, and contain olivine) have been interpreted as olivine-bearing basalts [*McSween et al.*, 2004; *Christensen et al.*, 2004c].

3.3. High Thermal Inertia, Morphologically Rough Unit

[32] This unit has similar thermal inertia to and coincides spatially with parts of the HTI_t unit of *Milam et al.* [2003] (i.e., with the "eastern lobe" of the large outcrop south of Thira and with discrete outcrops around the landing site), who interpreted it as consistent with very coarse sand to granule particle size.

[33] According to its thermophysical characteristics, the HTIR unit straddles between unit C of *Mellon et al.* [2000] and unit *F* of *Putzig et al.* [2004], and is therefore consistent with a mixture of rocks, bedrock, sand, and duricrust. Its surface morphology is etched, consistent with that of a relatively soft, slightly compacted, fine-grained material, strongly modified by wind erosion (Figure 11). The TES emissivity spectra of this unit show a type 1 (basaltic materials) signature (Figure 8). Toward the north, materials of this unit appear between mesas of homogeneous elevation up to 900 m across; the number and size of these mesas seem to increase toward the south and east of the external rim of Thira, where similar materials form continuous outcrops several km across. This observation may indicate the mesas are remnants of materials ejected from that crater.

[34] The largest outcrop of the HTIR unit is located south-southeast of Thira crater (Figure 11a). It occupies a mostly flat surface, 100 m above the rest of Gusev's floor (the only higher features in Gusev are the mesas near Ma'adim's debouchment, 300 m above Gusev's floor, followed by Thira's rim and adjacent mesas). Outcrops of similar etched morphology and high THEMIS thermal inertia occur near the landing site, in windows surrounded by the PM/LA units (Figure 10): to the east and northeast of Castril Crater (name provisionally approved by the WGPSN), centered at 14.69°S, 184.71°W (Figure 11c); in

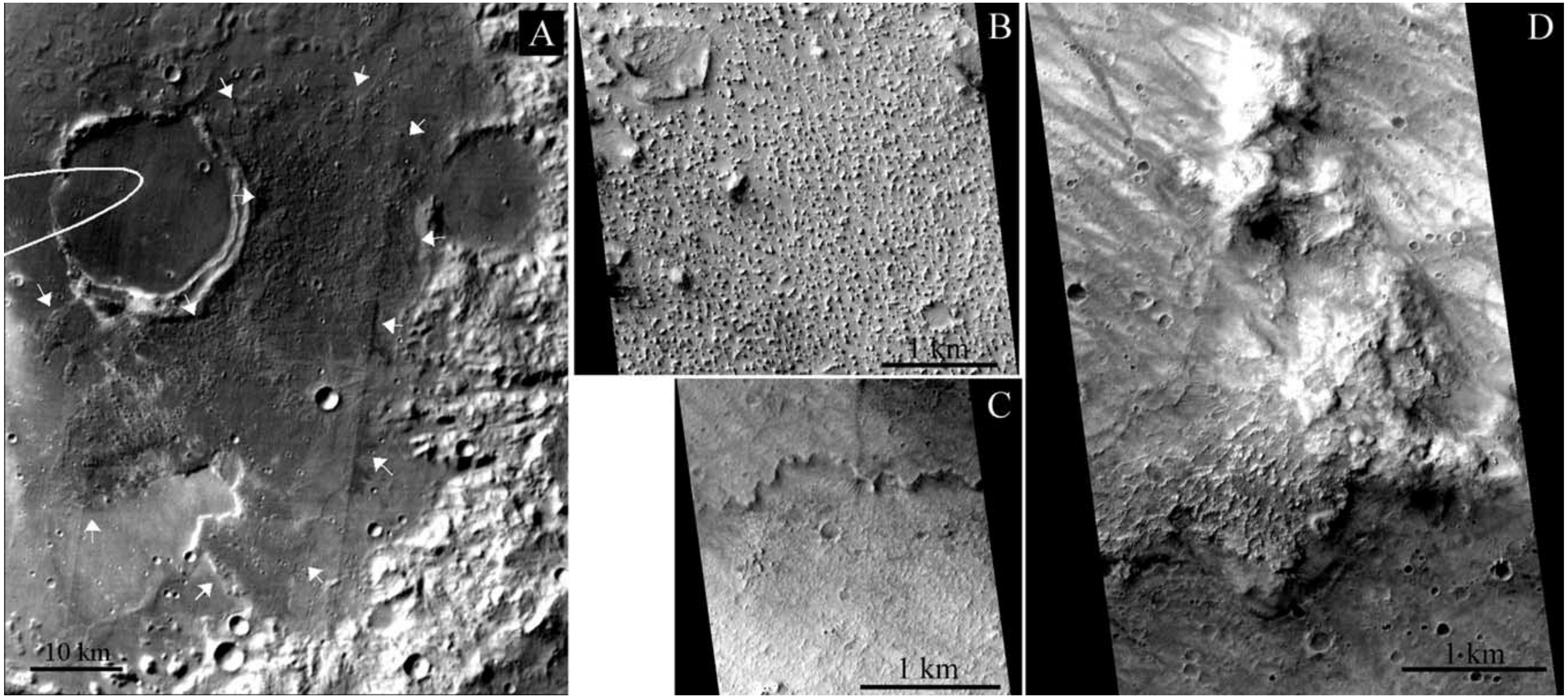

Figure 11. Morphologies characteristic of the HTIR unit. (a) Subset of THEMIS IR daytime radiance mosaic showing the largest outcrop of unit HTIR in Gusev, whose boundaries are indicated by arrows (part of the landing ellipse is shown for reference; cross indicates location of Figure 11b). (b) Subset of MOC scene E0201453 (centered at 14.88°S, 183.92°W). (c) Subset of MOC scene E0503287 (centered at 14.65°S, 184.64°W) showing the contact between PM/LA units (to the north) and HTIR materials (to the south); cliff is in average 15 m high, according to MOLA data. (d) Subset of MOC scene R0200357 (centered at 14.61°S, 184.47°W) showing the contact between PM/LA unit and HTIR materials (Columbia Hills).

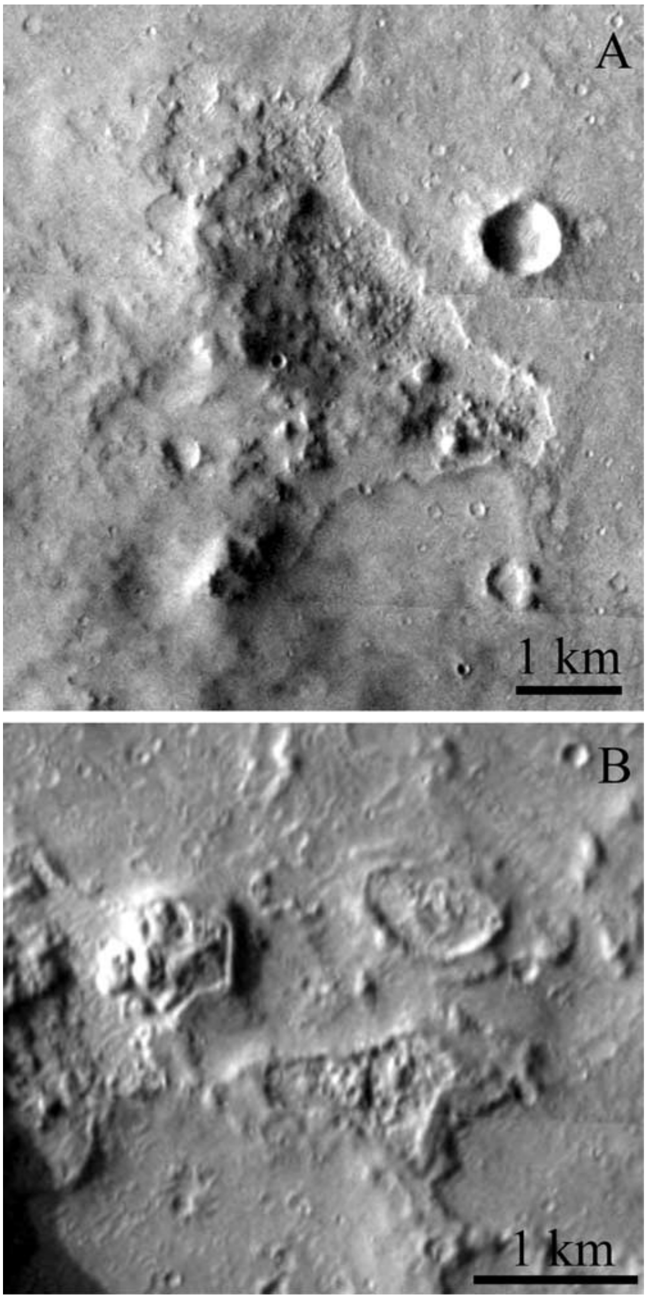

Figure 12. (a) Subsets of THEMIS visible images V06074002 (centered at 15.24°S, 185.27°W) and (b) V05325002 (centered at 15.51°S, 184.88°W), showing outcrops of unit HTIR through windows in the PM unit.

the Columbia Hills (Figure 11d); and in three other discrete outcrops south of the landing site (labeled O1, O2, and O3 in Figure 10). Three other windows in the PM unit showing underlying outcrops of similar morphology occur in the SW corner of Gusev (Figure 12), although their thermal inertia values at THEMIS resolution are only marginally higher than these of the surrounding plains. All of these outcrops, except for the Columbia Hills and the outcrop labeled O3, are topographically lower than the surrounding PM unit. In all the cases the Plains Material unit is superimposed onto the materials in these outcrops, indicating that the former is younger. The spatial dispersion of these outcrops could indicate that if indeed, all of them correspond to the same unit, the HTIR materials may be extensive in Gusev under the PM.

3.4. High Thermal Inertia, Morphologically Smooth Unit

[35] This unit coincides spatially with the ‘‘western lobe’’ of the HTI_t unit and with adjacent minor parts of the WR_t unit of *Milam et al.* [2003], interpreted by them as coarse sand to granule particle sizes and fine-grained sand, respectively.

[36] This unit presents locally the highest thermal inertia in the region and some of the lowest albedo values. According to its thermophysical properties, this unit straddles between units B of *Mellon et al.* [2000] and *F* of *Putzig et al.* [2004], and is therefore consistent with a surface covered with rocks, bedrock, sand, and some duricrust. The TES emissivity properties of this unit are consistent with these of type 1 materials, of basaltic composition.

[37] Outcrops of this unit appear mostly south of Thira. This unit presents superimposing and embayment relationships with materials from the HTIR unit; the continuous, lobated boundary between both units can be followed for tens of km (Figure 13a). Contrasting with the HTIR materials, this unit is morphologically smooth at THEMIS visible resolution; it consists of cliff-forming (therefore competent), layered materials (Figures 13b and 13c). At higher spatial resolution, it presents morphologies characteristic of terrestrial basaltic lava flows. Figure 14 shows an aerial photograph of a Hawaiian lava flow (Kalapana, Hawaii) and a MOC image corresponding to HTIS materials; both are at the same spatial scale. Flow-like features (scalloped or lobated, toe-like) are visible in the terrestrial picture (Figures 14c and 14d). These features are characteristic of pahoehoe lava flows advancing across flat or gentle slopes: series of small lobes and toes of magma break free from a cooled crust, forming these protuberances in the flow front. Analogous lobated and toe-like features, both in shape and scale, are present in the MOC image (Figures 14e and 14f).

3.5. Plains Materials Unit

[38] This unit coincides spatially with parts of the PL_t, WR_t, and ET_t units of *Milam et al.* [2003], interpreted, respectively, as surfaces covered by coarse sand, by fine-grained sand, and an erosional surface superimposed upon underlying material.

[39] The albedo and thermal inertia properties of the PM unit coincide with unit C of *Mellon et al.* [2000], and are therefore consistent with an indurated surface, mixed with some sand, rocks, and bedrock. The materials of this unit or these immediately beneath it are cliff forming (competent) (Figure 11c) and layered (Figure 11d); they overlay and embay the older materials of the HTIR unit (Figure 11c). Their surface morphology is smooth in general, disturbed only by craters and sinuous ridges. The PM are mantled by high albedo materials, which, when removed by dust devils, expose the LA unit. Small impact craters in the PM unit have contrasting, very high thermal inertia ejecta

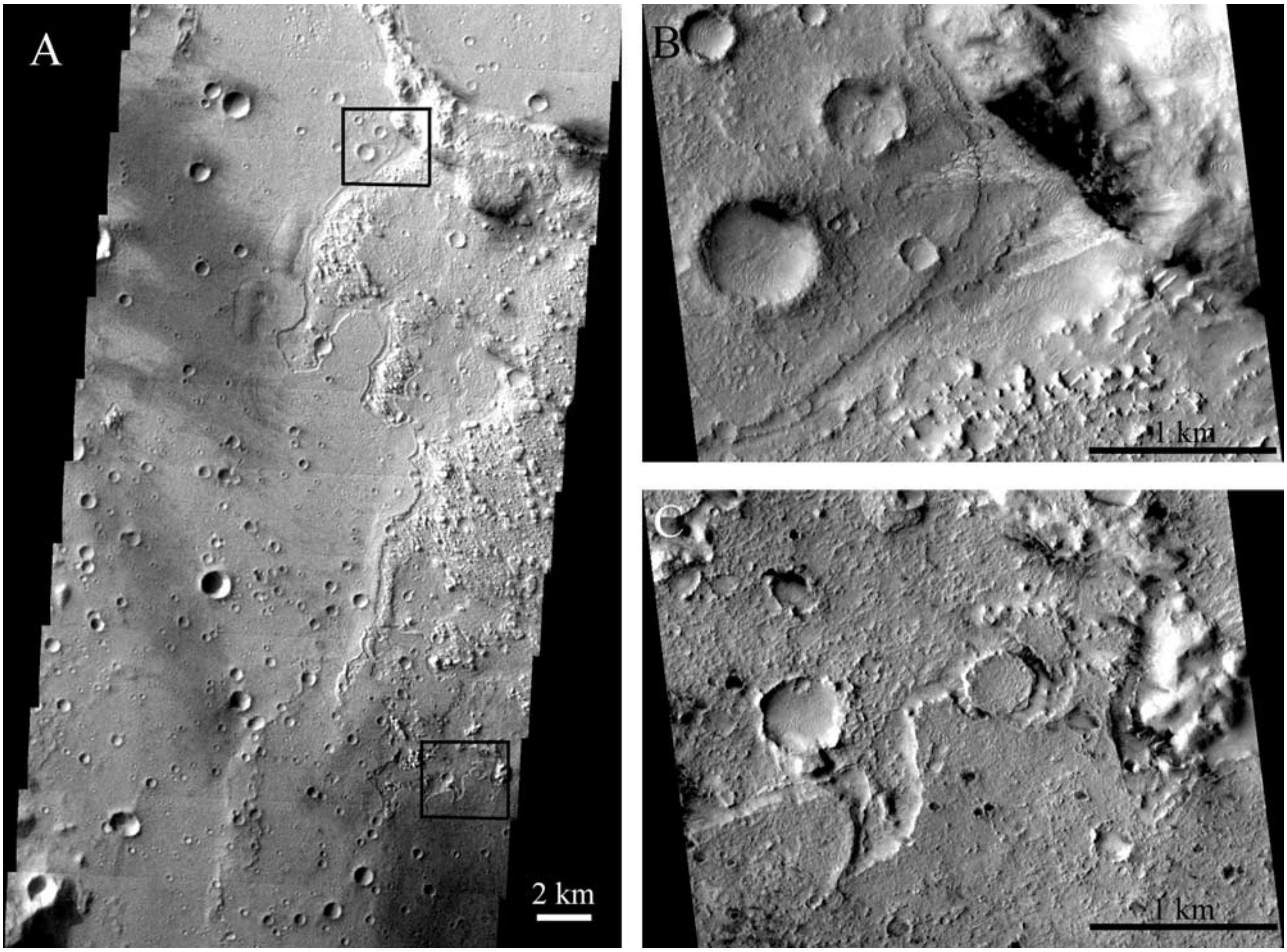

Figure 13. (a) Subset of THEMIS visible scene V04164003 showing contact between units HTIS and HTIR (boxes correspond to Figures 13b and 13c). At this scale there is no spatial or morphological discontinuity between units HTIS, PM, and LA. (b and c) Subsets of MOC narrow angle scene E0500471 showing layered, cliff-forming material of unit HTIS superimposed to materials of unit HTIR.

(Figures 3b and 6); this is consistent with the PM unit being a thin layer of intermediate thermal inertia overlying higher inertia materials. There is spatial and morphological continuity between this unit and the HTIS unit at THEMIS visible spatial resolution (Figure 13a). Basaltic materials have been detected remotely in LA/PM regions from TES emissivity (this study), and in situ by the spectrometers onboard MER-Spirit [*McSween et al.*, 2004; *Christensen et al.*, 2004c].

4. Discussion

[40] The oldest of the units proposed is, according to superposition criteria, the HTIR unit. The TES spectral properties of this unit are consistent with type 1 material, of basaltic composition. This unit could correspond to either volcanosedimentary or sedimentary deposits of basaltic composition strongly modified by wind erosion (e.g., etched and rough). Small outcrops of materials with similar morphology and, in some cases, similar thermophysical characteristics, occur in the center and southwest of Gusev, suggesting that this unit may be widespread, although covered by younger materials.

[41] Let us consider a scenario where materials of basaltic composition are transported either by wind or water from elsewhere and deposited in Gusev crater. Wind transportation and deposition would produce deposits very similar to those of volcanosedimentary origin; detailed petrographic analysis (to look for signs of particle reworking and for characteristic features such as volcanic bombs or fiamme, indicative of volcanosedimentary processes) would be required to rule out one origin in favor of the other. Water transportation and deposition would be expected to produce chemical weathering of the basaltic materials (e.g., primary

Figure 14. (a) Vertical aerial photograph showing the invasion of lava erupted by Kilauea volcano into Kalapana (Hawaii) (photograph credit: U.S. Geological Survey photograph by Dorian Weisel). (b) MOC visible narrow angle image E0500471 centered at 15.15°S, 184.10°W, corresponding to HTIS materials. Arrows point to flow-like features analogous in the two images both in morphology and scale and shown in detail in panels Figures 14c–14f. (c and d) Subsets of Figure 14a, showing lobated and toe-like features in the terrestrial lava flow. (e and f) Subsets of Figure 14b, showing flow-like features similar to these in Figures 14c and 14d, respectively.

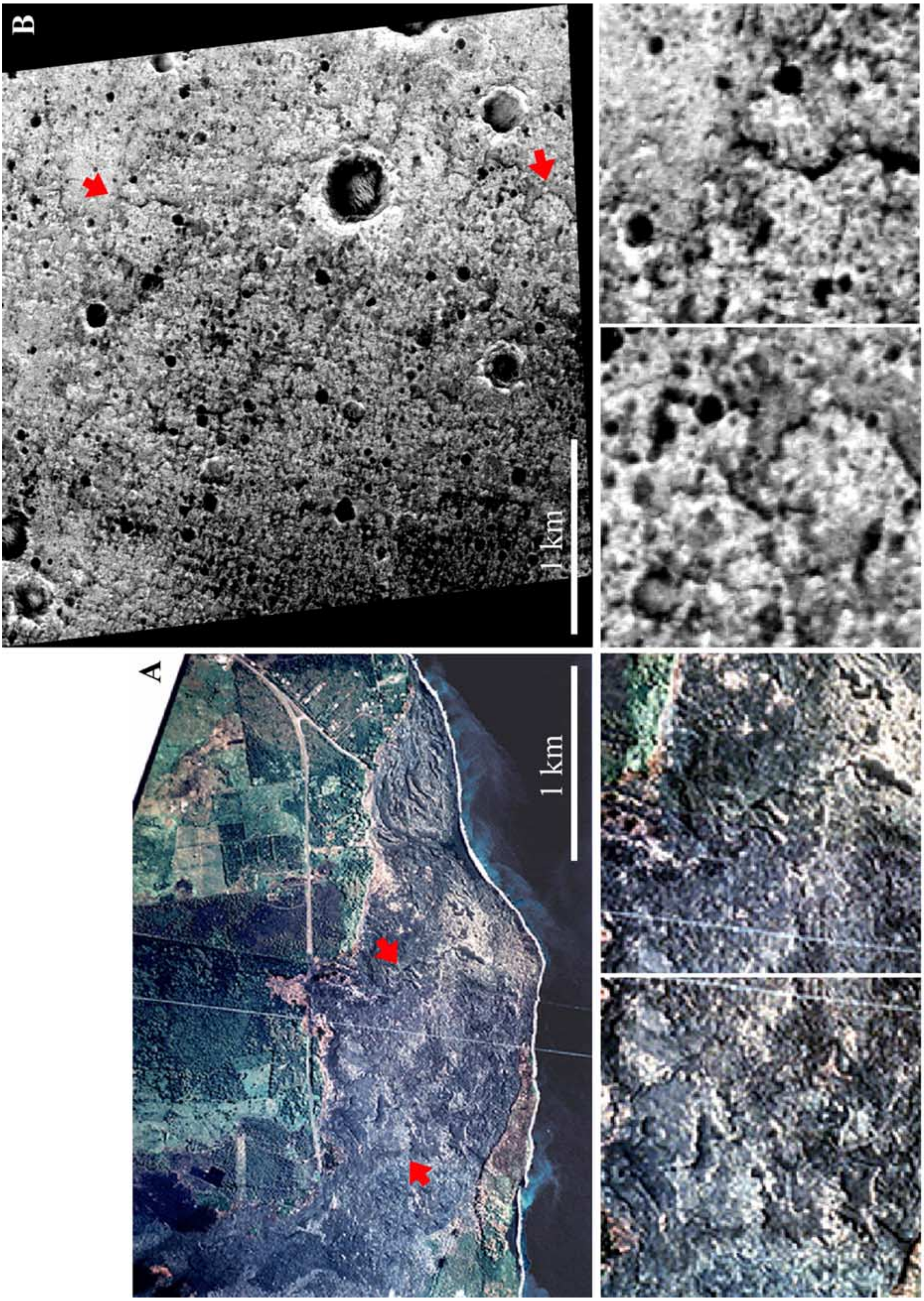

Figure 14

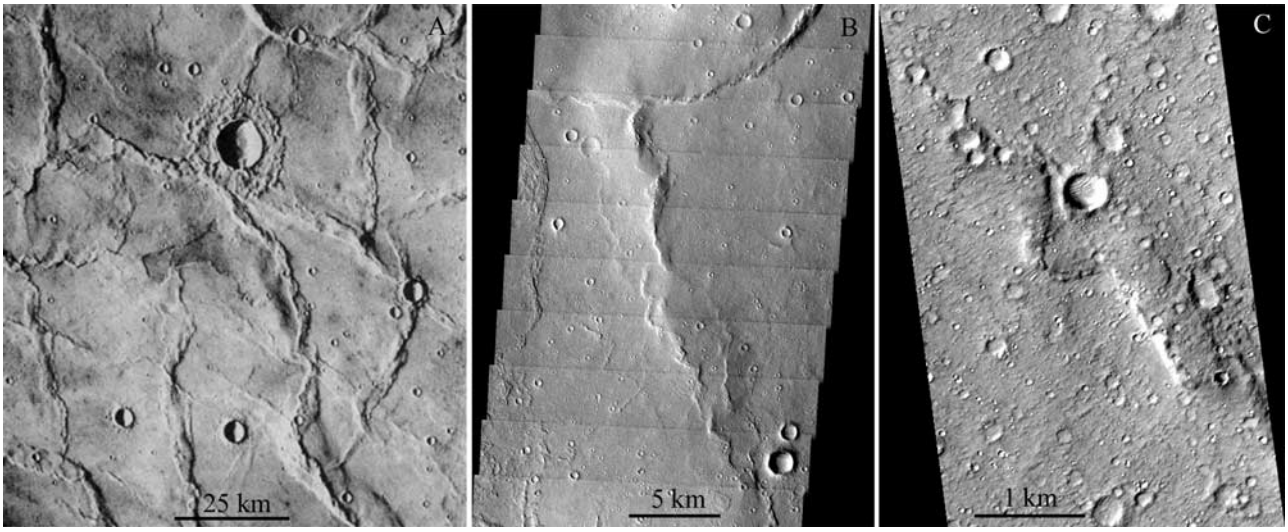

Figure 15. (a) Ridged plains in Hesperia Planum (NASA Viking Orbiter image 418539, north is to the top left; figure from *Mouginis-Mark et al.* [1992]) interpreted as volcanic in origin. (b) Subset of THEMIS visible scene V06798003, centered at 13.99°S, 184.57°W, showing examples of ridges at Gusev. (c) Subset of MOC scene M0301042, centered at 14.65°S, 184.97°W, showing detail of ridges at Gusev.

minerals such as olivine, pyroxene, and plagioclase would weather, producing phyllosilicates and iron oxides); ions liberated and put into solution by weathering would eventually cement the deposit, making it compact and more resistant to subsequent wind erosion.

[42] The presence of outcrops of similar etched morphology at different topographic heights underlying the HTIS and PM units across large distances would indicate that either (1) the original deposit was at least 150 m thick (from the averaged difference between the lowest and highest HTIR outcrops identified), occupied a large surface (on the order of 100 × 50 km), and was subsequently eroded to produce the topographic heights and lows we observe today, or (2) the original deposit was thinner, occupied a large surface, and covered preexisting topographic heights and lows. The former would be compatible with water deposition, the latter with wind deposition; present evidence does not allow for differentiation between the two.

[43] Lack of evidence of alteration minerals in the spectral data (no phyllosilicates or iron oxides were detected at the TES resolution), and morphological evidence indicative of relatively soft, unconsolidated, friable materials, heavily modified by wind erosion, favor a volcanosedimentary origin for the HTIR unit, or possibly aeolian deposition of preexisting volcanic materials eroded from elsewhere. While a water-laid sedimentation origin remains unlikely, it cannot be conclusively rejected with the evidence presently available.

[44] The HTIS unit overlays materials of the HTIR unit; the former is therefore younger. This unit has properties consistent with those of lava flows of basaltic composition: it has locally the darkest albedo in the region as well has the highest thermal inertia, consistent with dark rocky surfaces or dark bedrock; it presents lava flow morphologies as well as embayment relationships with an older unit (HTIR); it is cliff forming, denoting competent material; and has spectroscopic properties consistent with these of a basaltic material.

[45] The closeness of Apollinaris Patera, the presence of lava flows in the southern flank of this volcano, and the existence of a favorable path in the northwest of Gusev's rim (blocked at present by a young, unnamed impact crater) would argue for this volcano as a possible source for the flow. The estimated volume of volcanic material produced by Apollinaris Patera is in the order of 100,000 km^3 [*Robinson et al.*, 1993]; that needed to cover Gusev's floor with a 100-m-thick deposit is in the order of 4000 km^3.

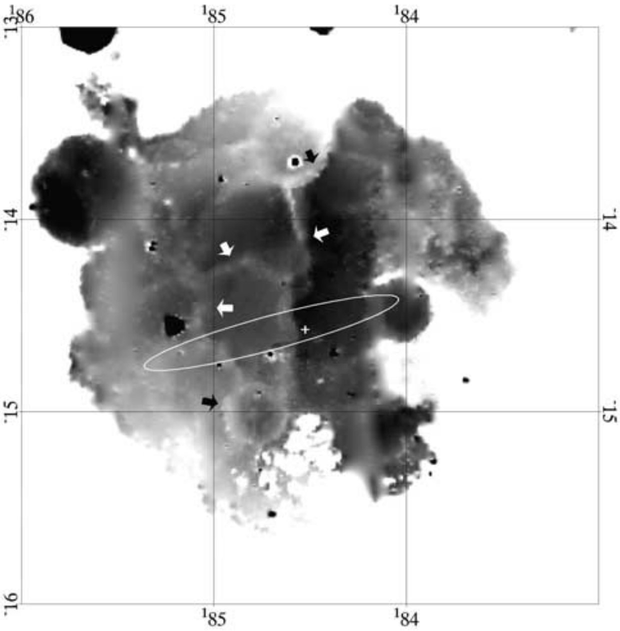

Figure 16. MOLA topographic data for the study area stretched to emphasize subtle features such as wrinkle ridges (white arrows) and quasi-circular depressions (black arrows). Lighter gray levels indicate higher elevations.

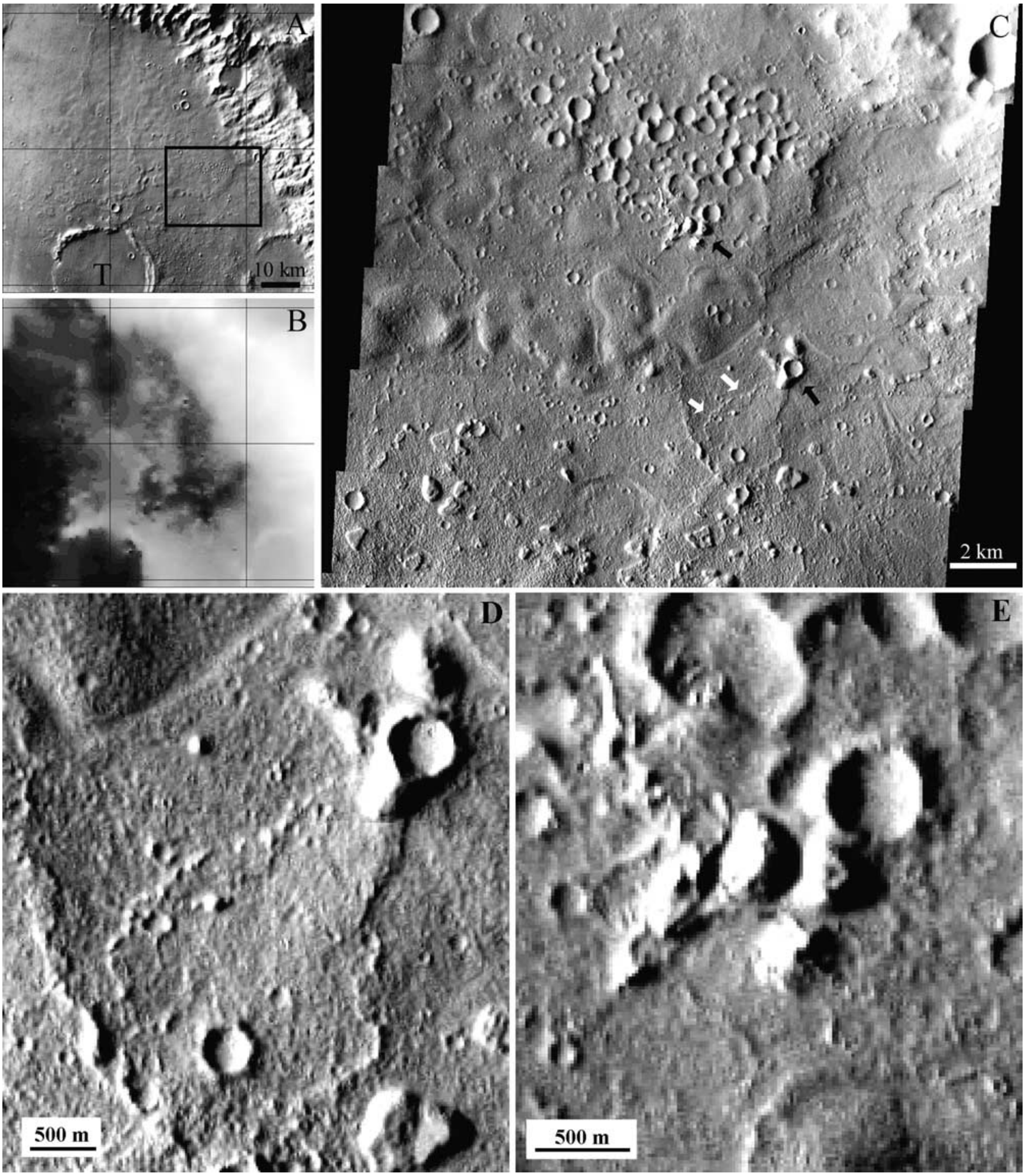

Figure 17. Examples of hummocky morphology and putative volcanic edifices. (a) Mosaic of THEMIS daytime brightness temperature centered near 14.00°S, 183.84°W; T: Thira crater; grid lines are 0.5° (approximately 30 km) on the side; box corresponds to Figure 17c. (b) Stretched MOLA topography for the same region, lighter shadows of gray indicate higher elevations. (c) Subset of THEMIS visible scene V05662001: black arrows indicate morphologies analogous to cinder cones (see Figures 17d and 17e for details), white arrows point to a possible volcanic flow (see Figure 17d for detail). (d and e) Detail.

From combined MOLA and MOC narrow-angle observations we conclude that, at least locally, the HTIS deposits may be as thin as 10–20 m (Figure 11c), which would require even lower volumes of volcanic material. Other sources of volcanism, such as fissures or small volcanic edifices, are equally viable.

[46] The PM unit has characteristics consistent with these of a regolith developed over basaltic lava flows: it has

intermediate thermal inertia and albedo, and presents spatial and morphological continuity at THEMIS visible scale with the HTIS unit. Very small (a few hundred meters in diameter) and therefore shallow impact craters in the PM unit have contrasting, very high thermal inertia ejecta; this is consistent with the presence of shallow underlying materials of higher thermal inertia. An alternative explanation is that the ejecta materials have higher thermal inertia because of their coarser particle size, maybe due to reduction of fines. Regolith formation may be due to physical weathering of basaltic materials by processes such as wind abrasion, thermal cycling, freeze thaw of interstitial water in cracks [*Sutter et al.*, 2004], and impact cratering.

[47] *Kuzmin et al.* [2000] recognized that a large portion of the materials in the floor of Gusev are morphologically analogous to those immediately north of the crater rim; they proposed a sedimentary origin for these materials (unit AHgf$_1$), while *Scott et al.* [1993] favored a volcanic origin (unit Ha$_4$). *Milam et al.* [2003] dated the plains materials at Gusev as Hesperian in age, which is also the age inferred for the Apollinaris Patera volcanism [*Robinson et al.*, 1993].

[48] Sinuous ridge morphologies are common in Gusev, mostly on the PM unit and on the transitional materials between this and the high thermal inertia units, although they also occur in the LA and LTI units. These ridges are evident both in THEMIS and MOC imagery (Figures 15b and 15c) and in MOLA topographic data (Figure 16). They are asymmetric in profile, with variable drop values (approximately from 50 to 5 m, depending on the ridge's scale) and orientation. Some ridges coincide spatially with quasi-circular depressions [*Kuzmin et al.*, 2000; *Milam et al.*, 2003], most probably buried craters. *Grin and Cabrol* [1997] detected in Viking "flat-topped, radially oriented" ridges in Gusev, and interpreted them as analogous to structures formed in terrestrial ice-covered lakes. Wrinkle ridges morphologically analogous to those observed in Gusev in the present study (Figure 15a) have been identified elsewhere associated with basaltic materials [*Solomon and Head*, 1979; *Watters*, 1988; *Mouginis-Mark et al.*, 1992] or with volcanic materials in general [*Ivanov and Head*, 2003]. These ridges may have formed in this region in response to basin loading by basalt fill [*Solomon and Head*, 1979], or as a manifestation of horizontal shortening [*Montesi and Zuber*, 2003].

[49] Hummocky morphology can be observed in one sector, northeast of Thira, occupied by PM, LTI, and transitional materials between these two units (Figure 17); this morphology is characterized by smooth, low (less than 20 m tall, according to MOLA data), rounded or elongated hills, 2 km or less across, in many cases alineated in the NS or EW direction. *Cabrol et al.* [2000], based on analysis of Viking data, interpreted some of these features as evidence for the presence of frost mounds (e.g., pingos). Higher resolution imagery fail to show the characteristic morphologies associated with terrestrial frost mounds; also, based on ice stability modeling [*Mellon and Jakosky*, 1993; *Mellon and Phillips*, 2001; *Mellon et al.*, 2004], ground ice would be presently unstable at any depth at Gusev. The spatial distribution, topographic slopes, and morphology of these intriguing features suggest flow (either debris flow or volcanic flow) in the NW to SE direction. The morphology and dimensions of these hummocky features are consistent with those of inflated lava flows (A. McEwen, personal communication, 2004). In terrestrial inflated pahoehoe sheet flows, as the magma advance slows, newly formed crust retains incoming lava, and the flow inflates, producing morphologies characterized by nearly horizontal upper surfaces and steep margins. Inflated flows on Kilauea and Mauna Loa (Hawaii) reach thicknesses in the 5–10 m range, and may be several kilometers long. When the internal pressure in the flow ruptures the crust, a new lobe forms. Lava tubes may develop, interconnecting series of lobes [*Hon et al.*, 1994]. Adjacent to some of these hummocky areas, THEMIS visible data (Figures 17c, 17d, and 17e) show small, positive relief features, some with a central crater and associated flow-like morphologies, which are suggestive of relatively younger cinder cones. A cluster of craters is also visible in the same region. It is possible that this is a cluster of secondary impact craters; the fact that they coincide with a topographically elevated area could indicate, though, that these may in fact be subdued, small volcanic edifices. High resolution MOC narrow-angle coverage for this region would be highly desirable to determine the nature of both the cinder cone-like features and clustered craters.

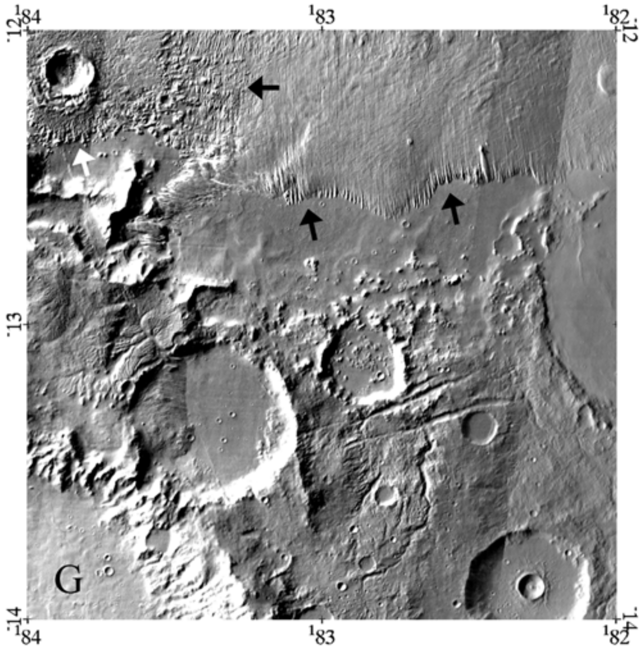

Figure 18. THEMIS daytime brightness temperature mosaic showing morphological features that indicate aeolian erosion of friable materials some 60 km north of Gusev Crater. G, Gusev Crater. Black arrows indicate yardang features, white arrow points to a pedestal crater.

[50] There is morphological continuity at THEMIS visible and MOC spatial resolution between the PM and LA units. The LA unit seems to correspond to PM devoid of blanketing, light-colored dust. The fact that the ranges of thermal inertia values of these two units are similar is consistent with this interpretation, since thermal inertia will be little affected by a very thin layer of dust. The rover Spirit landed in the LA unit; ground truth provided by Spirit indicates that this is a unit composed of angular, sometimes

faceted, basaltic blocks and locally indurated fine-grained materials, and is therefore consistent with our interpretation.

[51] The youngest materials identified in Gusev are these of the LTI unit, consisting of dust deposits blanketing underlying materials. The origin of this unit could be aeolian erosion and subsequent deposition of the volcanosedimentary materials located north and northeast of Gusev; these are friable materials, strongly modified by wind processes, as shown by the presence of nearby pedestal craters and well developed yardangs (Figure 18). Most surface materials in Gusev have an aeolian component, sometimes strong enough to obscure their thermophysical, spectroscopic, and morphological properties. This is the case of the mesas located in the mouth of Ma'adim Vallis, interpreted by other authors as remnants of an ancient delta [*Grin and Cabrol*, 1997].

5. Conclusions

[52] This three-way study of the properties of surface materials exposed at Gusev Crater has shed new light on the nature of past and present geological processes in the region. Analysis of TES spectroscopic data has allowed for the spatial mapping of the two dominant surface components in the region at the 3 by 6 km resolution: materials of basaltic composition and dust. This result is in agreement with previous analysis of the global Spectral Variance Index calculated from TES emissivity data [*Martínez-Alonso*, 2002; *Martínez-Alonso et al.*, 2003a, 2003b]; in those analyses, the Gusev region was found to have a very low spectral variance index (≤ 1), indicative of a spectrally bland surface coverage similar to that of the average of the planet.

[53] Analysis of presently available high spatial resolution data (MOC, THEMIS, MOLA) has shown that evidence previously interpreted as indicative of fluviolacustrine activity in Gusev (e.g., ridges formed by rotary currents, frost mounds) are instead more consistent with morphologies found in volcanic environments (wrinkle ridges and inflated lava sheet flows, respectively). Evidence indicating the possible presence of small volcanic edifices has also been identified. Analysis of TES- and THEMIS-derived thermal inertia and TES albedo has allowed for the determination of particle size, rock/bedrock exposure, and degree of induration; these properties have been used to constrain the physical character of the surface and the geological context of the materials identified from the analysis of the spectral and morphological data.

[54] We conclude that, at the scales of study allowed by the data presently available, the materials outcropping on the surface of Gusev Crater have properties consistent with those of volcanic deposits, modified by aeolian processes. The following units (listed according to their relative age), have been defined according to their thermophysical, spectral, and morphological properties: (unit HTIR) older deposits of basaltic composition strongly modified by wind erosion, possibly of volcanosedimentary origin or produced by aeolian deposition of preexisting volcanic materials eroded from elsewhere, though a sedimentary origin cannot be positively discarded at this point; (unit HTIS) lava flows of basaltic composition; (unit PM) a regolith developed from basaltic materials; (unit LA) that regolith locally devoid of blanketing dust by the action of dust devils; and (unit LTI) young aeolian deposits.

[55] Regions to be further analyzed in the future include: (1) HTIR unit outcrops, to elucidate if their origin is indeed volcanosedimentary or rather sedimentary, and to clarify if all the outcrops identified correspond to the same or to different units; (2) HTIS unit outcrops, to identify their source(s); (3) LTI unit outcrops of hummocky morphology, to analyze in detail features identified in this study as possible small volcanic edifices, and to investigate their relationship with the HTIS unit; and (4) the intriguing mesas in the mouth of Ma'adim Vallis, to clarify their character and origin. MER-Spirit data will be invaluable to clarify the character of the HTIR unit. High spatial resolution imaging (e.g., newly acquired MOC imagery, data from the Mars Express High Resolution Stereo Camera Images (HRSC) and the upcoming Mars Reconnaissance Orbiter High Resolution Imaging Science Experiment (MRO-HiRISE)) and spectroscopic data (e.g., data from Mars Express OMEGA and the upcoming Compact Reconnaissance Imaging Spectrometer for Mars (MRO-CRISM)) would be highly desirable to investigate the questions identified above.

[56] Fluviolacustrine processes proposed by other authors may have constituted an important part of the history of Gusev Crater; deposits produced by such processes may be found under the volcanic materials proposed here, or perhaps exposed in impact craters. Spectroscopic data of high spatial resolution (OMEGA, CRISM) of impact craters and their ejecta will either show the presence of the proposed fluviolacustrine materials or constrain the minimum thickness of the materials under which they may be found.

[57] **Acknowledgments.** We thank Josh Bandfield, Bob Pappalardo, and Bill Atkinson for helpful advice and discussions. Shannon Pelkey produced the albedo and TES thermal inertia maps utilized in this study. We thank Alfred McEwen and Brad Sutter for constructive reviews. Our appreciation to the science and operations teams responsible for the success of the Mars Global Surveyor and Mars Odyssey missions. This research was supported in part by the JPL Critical Products Data Analysis Program and by the Mars Data Analysis Program.

References

Bandfield, J. L. (2002), Global mineral distributions on Mars, *J. Geophys. Res.*, *107*(E6), 5042, doi:10.1029/2001JE001510.

Bandfield, J. L., V. E. Hamilton, and P. R. Christensen (2000), A global view of Martian surface composition from MGS-TES, *Science*, *287*, 1626–1630.

Boardman, J. W., and F. A. Kruse (1994), Automated spectral analysis: A geologic example using AVIRIS data, north Grapevine Mountains, Nevada, in *Proceedings 10th Thematic Conference on Geologic Remote Sensing*, pp. 407–418, Environ. Res. Inst. of Mich., Ann Arbor, Mich.

Boardman, J. W., F. A. Kruse, and R. O. Green (1995), Mapping target signatures via partial unmixing of AVIRIS data, *JPL Publ.*, *95-1*(1), 23–26.

Cabrol, N. A., E. A. Grin, A. Dollfus, and G. Dawidowicz (1993), An ancient inner lake in Ma'adim Vallis, in *Proceedings XXIV Lunar and Planetary Science Conference*, pp. 241–242, Lunar and Planet. Inst., Houston, Tex.

Cabrol, N. A., E. A. Grin, R. Landheim, R. O. Kuzmin, and R. Greeley (1998), Duration of the Ma'adim Vallis/Gusev Crater hydrologic system, Mars, *Icarus*, *133*, 98–108.

Cabrol, N. A., E. A. Grin, and W. H. Pollard (2000), Possible frost mounds in an ancient Martian lake bed, *Icarus*, *145*, 91–107.

Christensen, P. R., et al. (1992), Thermal emission spectrometer experiment: Mars observer mission, *J. Geophys. Res.*, *97*(E5), 7719–7734.

Christensen, P. R., J. L. Bandfield, V. E. Hamilton, D. A. Howard, M. D. Lane, J. L. Piatek, S. W. Ruff, and W. L. Stefanov (2000), A thermal emission spectral library of rock-forming minerals, *J. Geophys. Res.*, *105*(E4), 9735–9739.

Christensen, P. R., R. V. Morris, M. D. Lane, J. L. Bandfield, and M. C. Malin (2001), Global mapping of Martian hematite mineral deposits: Remnants of water-driven processes on early Mars, *J. Geophys. Res.*, *106*(E10), 23,873–23,885.

Christensen, P. R., et al. (2003), Morphology and composition of the surface of Mars: Mars Odyssey THEMIS results, *Science*, *300*, 2056–2061.

Christensen, P. R., et al. (2004), The Thermal Emission Imaging System (THEMIS) for the Mars 2001 Odyssey mission, *Space Sci. Rev.*, *118*, 85–130.

Christensen, P., et al. (2004c), Initial results from the Mini-TES experiment in Gusev Crater from the Spirit Rover, *Science*, *305*, 837–842.

Eliason, E. M. (1997), Production of digital image models using the ISIS system, paper presented at XXVIII Lunar and Planetary Science Conference, Lunar and Planet. Inst., NASA Johnson Space Cent., Houston, Tex.

Gaddis, L., et al. (1997), An overview of the integrated software for imaging spectrometers (ISIS), paper presented at XXVIII Lunar and Planetary Science Conference, Lunar and Planet. Inst., NASA Johnson Space Cent., Houston, Tex.

Greeley, R., and J. E. Guest (1987), Geologic map of the eastern equatorial region of Mars, *Map I-1802-B 1:15,000,000*, U.S. Geol. Surv., Reston, Va.

Green, A. A., M. Berman, P. Switzer, and M. D. P. Craig (1988), A transformation for ordering multispectral data in terms of image quality with implications for noise removal, *IEEE Trans. Geosci. Remote Sens.*, *26*, 65–74.

Grin, E. A., and N. A. Cabrol (1997), Limnologic analysis of Gusev Crater paleolake, Mars, *Icarus*, *130*, 461–474.

Hon, K., J. Kauahikaua, R. Denlinger, and K. Mackay (1994), Emplacement and inflation of pahoehoe sheet flows: Observations and measurements of active lava flows on Kilauea Volcano, Hawaii, *Geol. Soc. Am. Bull.*, *106*, 351–370.

Irwin, R. P., T. A. Maxwell, A. D. Howard, R. A. Craddock, and D. W. Leverington (2002), A large paleolake basin at the head of Ma’adim Vallis, Mars, *Science*, *296*, 2209–2212.

Ivanov, M. A., and J. W. Head (2003), Syrtis Major and Isidis Basin contact: Morphological and topographic characteristics of Syrtis Major lava flows and material of the Vastitas Borealis Formation, *J. Geophys. Res.*, *108*(E6), 5063, doi:10.1029/2002JE001994.

Jakosky, B. M. (1986), On the thermal properties of Martian fines, *Icarus*, *66*, 117–124.

Jakosky, B. M., and M. T. Mellon (2001), High-resolution thermal inertia mapping of Mars: Sites of exobiological interest, *J. Geophys. Res.*, *106*(E10), 23,887–23,907.

Kieffer, H. H., S. C. Chase, E. Miner, G. Munch, and G. Neugebauer (1973), Preliminary report on infrared radiometric measurements from the Mariner 9 spacecraft, *J. Geophys. Res.*, *78*, 4291–4312.

Kruse, F. A., A. B. Lefkoff, J. W. Boardman, K. B. Heidebrecht, A. T. Shapiro, P. J. Barloom, and A. F. H. Goetz (1993), The spectral image processing system (SIPS)–Interactive visualization and analysis of imaging spectrometer data, *Remote Sens. Environ.*, *44*, 145–163.

Kuzmin, R. O., R. Greeley, R. Landheim, N. A. Cabrol, and J. D. Farmer (2000), Geologic map of the MTM-15182 and MTM-15187 quadrangles, Gusev Crater-Ma’adim Vallis region, Mars, *Map I-2666*, U.S. Geol. Surv., Reston, Va.

Malin, M. C., G. E. Danielson, A. P. Ingersoll, H. Masursky, J. Veverka, M. A. Ravine, and T. A. Soulanille (1992), Mars-Observer camera, *J. Geophys. Res.*, *97*(E5), 7699–7718.

Martínez-Alonso, S. (2002), Mineralogical mapping of Mars using data-derived end-members, paper presented at Astrobiology Science Conference 2002, NASA Ames Res. Cent., Moffit Field, Calif.

Martínez-Alonso, S., B. C. Kindel, M. T. Mellon, and B. M. Jakosky (2003a), Spectral variance derived from MGS-TES data as a tool to detect hydrothermal systems, paper presented at XXXIV Lunar and Planetary Science Conference, Lunar and Planet. Inst., NASA Johnson Space Cent., Houston, Tex.

Martínez-Alonso, S., B. C. Kindel, and M. T. Mellon (2003b), Analysis of areas of high spectral variance detected in TES data, paper presented at NASA Astrobiology Institute General Meeting, Ariz. St. Univ., Tempe, Ariz., 10–12 Feb.

McSween, H. Y., et al. (2004), Basaltic rocks analyzed by the Spirit Rover in Gusev Crater, *Science*, *305*, 842–845.

Mellon, M. T., and B. M. Jakosky (1993), Geographic variations in the thermal and diffusive stability of ground ice on Mars, *J. Geophys. Res.*, *98*(E2), 3345–3364.

Mellon, M. T., and R. J. Phillips (2001), Recent gullies on Mars and the source of liquid water, *J. Geophys. Res.*, *106*(E10), 23,165–23,179.

Mellon, M. T., B. M. Jakosky, H. H. Kieffer, and P. R. Christensen (2000), High-resolution thermal inertia mapping from the Mars Global Surveyor Thermal Emission Spectrometer, *Icarus*, *148*, 437–455.

Mellon, M. T., W. C. Feldman, and T. H. Prettyman (2004), The presence and stability of ground ice in the southern hemisphere of Mars, *Icarus*, *169*, 324–340.

Milam, K. A., K. R. Stockstill, J. E. Moersch, H. Y. McSween Jr., L. L. Tornabene, A. Ghosh, M. B. Wyatt, and P. R. Christensen (2003), THEMIS characterization of the MER Gusev crater landing site, *J. Geophys. Res.*, *108*(E12), 8078, doi:10.1029/2002JE002023.

Montesi, L. G. J., and M. T. Zuber (2003), Clues to the lithospheric structure of Mars from wrinkle ridge sets and localization instability, *J. Geophys. Res.*, *108*(E6), 5048, doi:10.1029/2002JE001974.

Mouginis-Mark, P. J., L. Wilson, and M. T. Zuber (1992), The physical volcanology of Mars, in *Mars*, edited by H. H. Kieffer et al., pp. 424–452, Univ. of Ariz. Press, Tucson, Ariz.

Palluconi, F. D., and H. H. Kieffer (1981), Thermal inertia mapping of Mars from 60°S to 60°N, *Icarus*, *45*, 179–201.

Presley, M. A., and P. R. Christensen (1997), Thermal conductivity measurements of particulate materials: 2. Results, *J. Geophys. Res.*, *102*(E3), 6551–6566.

Putzig, N. E., M. T. Mellon, K. A. Kretke, and R. E. Arvidson (2004), Global thermal inertia and surface properties of Mars from the MGS mapping mission, *Icarus*, in press.

Rice, J. W., and P. R. Christensen (2003), THEMIS observations, discoveries and predictions for the MER A landing site in Gusev Crater, *Eos Trans. AGU*, *84*(46), Fall Meet. Suppl., Abstract P21C-02.

Robinson, M. S., P. J. Mouginis-Mark, J. R. Zimbelman, S. S. C. Wu, K. K. Ablin, and A. E. Howington-Kraus (1993), Chronology, eruption duration, and atmospheric contribution of the Martian volcano Apollinaris Patera, *Icarus*, *104*, 301–323.

Schneeberger, D. M. (1989), Episodic channel activity at Ma’adim Vallis, Mars, in *Proceedings XX Lunar and Planetary Science Conference*, pp. 964–965, Lunar and Planet. Inst., Houston, Tex.

Scott, D. H., and K. L. Tanaka (1982), Ignimbrites of the Amazonian Planitia region on Mars, *J. Geophys. Res.*, *87*, 178–190.

Scott, D. H., E. C. Morris, and M. N. West (1978), Geologic map of the Aeolis quadrangle of Mars, *Map I-1111 1:5,000,000*, U.S. Geol. Surv., Reston, Va.

Scott, D. H., J. M. Dohm, and D. J. Applebee (1993), Geologic map of science study area 8, Apollinaris Patera Region of Mars (special MTM–10,186 quadrangle), U.S. Geol. Surv., Reston, Va.

Seidelmann, P. K., et al. (2002), Report of the IAU/IAG working group on cartographic coordinates and rotational elements of the planets and satellites: 2000, *Celestial Mech. Dyn. Astron.*, *82*, 83–110.

Smith, M. D., J. L. Bandfield, and P. R. Christensen (2000), Separation of atmospheric and surface spectral features in Mars Global Surveyor Thermal Emission Spectrometer (TES) spectra, *J. Geophys. Res.*, *105*(E4), 9589–9607.

Smith, M. D., J. C. Pearl, B. J. Conrath, and P. R. Christensen (2001), Thermal Emission Spectrometer results: Mars atmospheric thermal structure and aerosol distribution, *J. Geophys. Res.*, *106*(E10), 23,929–23,945.

Solomon, S. C., and J. W. Head (1979), Vertical movement in Mare basins: Relation to Mare emplacement, basin tectonics, and lunar thermal history, *J. Geophys. Res.*, *84*(B4), 1667–1682.

Sutter, B., J. M. Moore, and A. P. Zent (2004), Examining the sediments and soils of Gusev Crater with the Athena science payload, *J. Geophys. Res.*, *109*, E04002, doi:10.1029/2003JE002157.

Torson, J. M., and K. J. Becker (1997), ISIS—A software architecture for processing planetary images, paper presented at XXVIII Lunar and Planetary Science Conference, Lunar and Planet. Inst., NASA Johnson Space Cent., Houston, Tex.

Watters, T. H. (1988), Wrinkle ridge assemblages on the terrestrial planets, *J. Geophys. Res.*, *93*(B9), 10,236–10,254.

Zuber, M. T., D. E. Smith, S. C. Solomon, D. O. Muhleman, J. W. Head, J. B. Garvin, J. B. Abshire, and J. L. Bufton (1992), The Mars-Observer Laser Altimeter investigation, *J. Geophys. Res.*, *97*(E5), 7781–7797.

B. M. Jakosky and N. E. Putzig, Department of Geological Sciences, University of Colorado, Boulder, CO 80309, USA.

S. Martínez-Alonso and M. T. Mellon, Laboratory for Atmospheric and Space Physics, University of Colorado, Campus Box 392, Boulder, CO 80309, USA. (martinas@lasp.colorado.edu)